Non-canonical role for the BAF complex subunit DPF3 in mitosis and ciliogenesis

Giulia Verrillo[1], Anna Maria Obeid[1], Alexia Genco[1], Jacopo Scrofani[2], François Orange[3], Sarah Hanache[1], Julien Mignon[4], Tanguy Leyder[4], Catherine Michaux[4], Céline Kempeneers[5,6], Noëmie Bricmont[5,6], Stephanie Herkenne[7], Isabelle Vernos[2,8,9], Maud Martin[10] and Denis Mottet[1,*]

[1]University of Liege, GIGA – Research Institute, Molecular Analysis of Gene Expression (MAGE) Laboratory, B34, Avenue de l'Hôpital, B-4000 Liège, Belgium
[2]Centre for Genomic Regulation (CRG), The Barcelona Institute of Science and Technology, Barcelona, Spain
[3]Université Côte d'Azur, Centre Commun de Microscopie Appliquée (CCMA), 06100 Nice, France
[4]University of Namur, Laboratory of Physical Chemistry of Biomolecules, Unité de Chimie Physique Théorique et Structurale (UCPTS), Rue de Bruxelles 61, B-5000 Namur, Belgium.
[5]University of Liege, Pneumology Laboratory, I3 Group, GIGA Research Center, B-4000 Liège, Belgium
[6]Division of Respirology, Department of Pediatrics, University Hospital Liège, B-4000 Liège, Belgium
[7]University of Liege, GIGA-Cancer, Laboratory of Mitochondria and Cell Communication, B34, Avenue de l'Hôpital, B-4000 Liège, Belgium.
[8]Universitat Pompeu Fabra (UPF), Barcelona, Spain
[9]ICREA, Pg. Lluis Companys 23, Barcelona 08010, Spain
[10]Laboratory of Neurovascular Signaling, Department of Molecular Biology, ULB Neuroscience Institute, Université libre de Bruxelles, B-6041 Gosselies, Belgium

[*]Corresponding Author: Denis MOTTET, PhD

Molecular Analysis of Gene Expression (MAGE) Laboratory, GIGA, University of Liège, GIGA Building, B34, +1, B-4000 Liège, Belgium

Tel: +32 4366-4422

E-mail: dmottet@uliege.be

Highlights

- **DPF3 localizes in centriolar satellites, spindle midzone/bridging fiber area and midbodies**
- **DPF3 ensures mitosis completion and maintains genomic stability**

- **DPF3 is required for K-fiber stability, KT–MT attachment and chromosome alignment**
- **DPF3 is a centriolar satellite protein involved in primary ciliogenesis**

Abstract

DPF3, along with other subunits, is a well-known component of the BAF chromatin remodeling complex that plays a key role in regulating chromatin remodeling activity and gene expression. Here, we elucidated a non-canonical localization and role for DPF3. We showed that DPF3 dynamically localizes to the centriolar satellites in interphase and in centrosome, spindle midzone/bridging fiber area and midbodies during mitosis. Loss of DPF3 causes K-fiber instability, unstable kinetochore-microtubules attachment and defects in chromosome alignment, thus resulting in altered mitotic progression, cell death and genomic instability. In addition, we also demonstrated that DPF3 localizes in centriolar satellites at the basis of primary cilia and is required for ciliogenesis by regulating axoneme extension. Together, these findings uncover a moonlighting dual function for DPF3 during mitosis and ciliogenesis.

Keywords: DPF3 – Chromosome alignment – Bridging Fiber – Mitosis – Genomic instability – Centriolar satellites – Ciliogenesis.

Introduction

The BAF (BRG1/BRM-associated factor) complex, the mammalian homolog of the yeast SWI/SNF complex, is one of the four mammalian ATP-dependent chromatin remodeling complex families (Ho and Crabtree, 2010)(Kadoch and Crabtree, 2015). The core of the BAF complex is composed of an ATPase catalytic subunit (either Brg1 or Brm) and at least SMARCE1/BAF57, ACTL6A/BAF53, SMARCC1/BAF155, SMARCC2/BAF170 and SMARCB1/SNF5/BAF47. These core subunits are responsible for essential chromatin remodeling activity (Yan et al., 2017). However, hundreds of distinct BAF complexes are predicted to form *in vivo* through combinatorial assembly (Ho and Crabtree, 2010). Based on the combination of additional non-core BAF subunits, BAF complexes have unique and specific composition in certain tissue/cell types to perform a specialized function.

SKIFt in isoforms of non-core BAF complex subunits is important for the transition from a precursor to a differentiated state during neural and muscle differentiation. For instance, the neural precursor BAF complex (npBAF) in neural progenitor cells is composed of BAF53a and BAF45a. After mitosis and differentiation, these subunits are substituted by BAF53b, BAF45b or BAF45c and form the neural BAF complexes (nBAF) (Lessard et al., 2007). Similarly, BAF45c is a specific component of the cardiac BAF complex (CBAF), which is essential for heart and muscle development.

Even if there has been an enormous gain in understanding how BAF complexes assemble and function, the role of distinct non-core subunits remains poorly understood. Despite its essential role in neural development, very little is known about the role and mechanisms of action of the auxiliary BAF45c subunit in other tissues or cell types.

In human BAF45c, also named DPF3 (Double-PHD fingers 3) or CERD4, exists as two isoforms: DPF3b and DPF3a. DPF3b is characterized by a tandem of PHD (plant homeobox domain) zinc fingers (ZnFs) at its C-terminus extremity. These structural features enable DPF3b to bind acetylated or methylated histones on the chromatin, hence acting as a histone reader in the BAF complex (Lange et al., 2008)(Zeng et al., 2010). Unlike DPF3b, DPF3a has a single truncated PHD ZnF (PHD-1/2) and is therefore unable to bind modified histones. Nonetheless, DPF3a is involved in myogenic differentiation by interacting with the hepatoma-derived growth factor-related protein 2 (HRP2). Formation of DPF3a-HRP2 complex facilitates the association of HRP2 with BAF, leading to the transcription of myogenic gene (Zhu et al., 2020). Cardiac gene transcription has also found to be regulated by DPF3a through phosphorylation of its C-terminal domain and interaction with the transcriptional repressors HEY (HES-related repressor protein). The BAF complex is thereafter recruited by the DPF3a-HEY complex, triggering the transcription of fetal genes, which promotes cardiac hypertrophy (Cui et al., 2016).

Both DPF3a and DPF3b are intrinsically disordered proteins (IDPs) (Mignon et al., 2021)(Mignon et al., 2022)(Leyder et al., 2022). The two isoforms have a high disorder content, lack a hydrophobic core, and display a context-dependent expanded and/or collapsed conformational ensemble. DPF3a is more disordered than DPF3b due to the presence of an additional intrinsically disordered region (IDR) at its C-terminus. The flexibility of IDPs is exploited in their biological function and, in

many instances, allows a single IDP to interact with multiple proteins and regulate a broad range of biological processes. Our recent characterization of the disordered nature of DPF3 isoforms is highly pertinent (Mignon et al., 2021)(Mignon et al., 2022)(Leyder et al., 2022) and drives us for a better understanding of its functionality. We therefore aimed to determine whether DPF3 might exert unexpected roles beyond its well-established function in regulating BAF complex.

Our present study reveals that the DPF3 protein was surprisingly found to dissociate from the BAF-SWI/SNF chromatin remodeling complex during mitosis and play an unexpected direct role in cell division. DPF3 is spatiotemporally located into three distinct complex structures, including the centriolar satellites, the spindle midzone/bridging fiber area as well as the midbody. Looking at the cellular importance of DPF3, we found that depletion of DPF3 induced cell cycle blocking in M phase and subsequent apoptotic cell death, suggesting that localization of DPF3 to mitotic structures is essential for proper mitotic division and genomic stability. Mechanistically, we demonstrated that DPF3 depletion causes kinetochore-fiber (K-fiber) instability, less stable kinetochore – microtubules (KT–MT) attachment and defects in chromosome alignment at the metaphase plate. Furthermore, we unveiled the localization of DPF3 at the basal body of the primary cilium in quiescent vertebrate cells. Depletion of DPF3 dramatically arrests primary ciliogenesis at the initial step of axoneme extension. Altogether, the results uncover a novel dual role for DPF3 in mitosis and ciliogenesis.

Results

DPF3 is a centriolar satellites- associated protein

To identify the subcellular localization of DPF3, we first started by looking at its presence along with individual BAF subunits in U2OS cells using a chromatin-enriched fractionation. While most of the subunits are predominantly present in the chromatin-enriched fraction, DPF3 was observed equally distributed in the cytoplasm and nuclear fraction (**Fig. 1A**). Two bands are observed in the chromatin-enriched fraction. Since our DPF3 antibodies recognize both DPF3a and DPF3b isoforms, we hypothesized that the lower band corresponds to the DPF3a isoform according to its theoretical molecular weight (38 kDa) and the upper band to DPF3b isoform with a molecular weight of 42 kDa. On contrary, only the lower band is observed in the

cytoplasmic and soluble nuclear fractions, suggesting that only DPF3a is present in this cellular compartment in this cell type.

To evaluate whether DPF3 interacts with the core ATPase BAF subunits Brg1 or Brm in U20S cells, we performed co-immunoprecipitation (Co-IP) experiments with antibodies against Brg1 or Brm. While we found out that the core subunit BAF170 was physically associated with Brg1/Brm, DPF3 was not present in the ATPase Brg1/Brm-based complexes (**Figs. 1B, 1C**), suggesting that, at least in U2OS cells, DPF3 is not associated with the ATPase BAF subunits and may act independently.

In the light of the detected presence of DPF3 in the cytoplasmic fraction, we next further investigated the subcellular localization of endogenous DPF3 by immunofluorescence after cold methanol/acetone fixation and staining with an antibody recognizing both DPF3a/b isoforms. In interphase, DPF3 was detected in the nuclear compartment. Surprisingly, a DPF3 staining as small granules reminiscent to centrosome structure was also observed in the cytoplasm (**Fig. 1D and Figs. S1A**). To better visualize centrosomal localization of endogenous DPF3, cells were pre-incubated with CSK extraction buffer prior to fixation with acetone/methanol to remove soluble proteins and enable detection of the insoluble proteins that are anchored to cellular structures. Immunofluorescence microscopy revealed DPF3 staining at centrosome-like structures, as well as bright foci in the nuclear compartment in interphasic cells. To validate the presence of DPF3 in the centrosomal compartment, endogenous DPF3 was co-stained with the common centrosome marker γ-tubulin. Confocal microscopy analysis revealed that DPF3 co-localizes with γ-tubulin confirming that DPF3 is indeed present in the centrosomal compartment (**Fig**. **1E)**. As an additional way to firmly determine for the presence of endogenous DPF3 at centrosomes, we also performed immunofluorescence on purified centrosomes. The majority of them co-reacted with anti-DPF3 and anti-γ-tubulin antibodies, thus confirming the presence of DPF3 in centrosome (**Fig**. **1F)**. Transfection of two different siRNAs (siDPF3 #1 and siDPF3 #2) targeting both DPF3a and DPF3b isoforms, which significantly reduced DPF3 expression at both mRNA and protein level **(Figs. S1B, S1C**), abrogated DPF3 staining in the vicinity of the centrosome (**Fig. S1D**). This result validates the specificity of the anti-DPF3 antibody used in immunofluorescence experiments. Interestingly, no centrosomal signal was detected for Brm or Brg1 that are exclusively nuclear, suggesting that

centrosomal localization of DPF3 was independent of the core BAF complex (**Figs. S1E, S1F**). In addition, DPF3 showed centrosomal localization in several other cell lines including HeLa, MDA-MB 231, T47D and MCF7 cells (**Fig. S1G**).

Centrosomes are composed of a pair of centrioles surrounded by amorphous pericentriolar material (PCM) and small membrane-less granules called centriolar satellites. To more precisely determine the localization of DPF3 in these structures, immunofluorescence experiments were performed in both U2OS and HeLa cells using centrin, γ-tubulin or PCM1 antibodies to respectively label the centrioles (Salisbury et al., 2002), the pericentriolar matrix (Baumann, 2012) and the centriolar satellites (Hall et al., 2023a). High-resolution (HR) microscopy analyses showed no co-localization of DPF3 with centrin, suggesting that DPF3 is not present in centrioles. A very faint staining with γ-tubulin was seen by HR, suggesting that DPF3 is not highly abundant in the pericentriolar matrix. Remarkably, DPF3 and PCM1 co-localize almost perfectly, leading us to conclude that DPF3 is strictly a centriolar satellite protein (**Fig**. **1G and Fig. S2A and S2B**).

The pericentrosomal distribution of centriolar satellite proteins depends on an intact microtubule network (Conkar et al., 2019). The disruption of microtubule network by nocodazole treatment leads to a substantial decrease in the amount of the granular DPF3 staining located around the centrosome (**Fig.1H**). This observation suggests that the major fraction of DPF3 localizes to centriolar satellites. Finally, Co-IP experiment revealed that DPF3 interacts with PCM1; further supporting that DPF3 is a centriolar satellite protein (**Fig.1I**).

DPF3 is located in centrosomal compartment, spindle midzones/bridging fiber area and midbodies during mitosis

The centrosome is a dynamic structure that plays important cellular role during mitosis. We therefore assessed whether DPF3 co-localizes with centrosomes throughout the stages of cell cycle. In G1 and S phase, DPF3 staining is present around the centriole core in an irregular PCM1-like pattern. Mitotic cells were identified based on nuclear condensation patterns representative of each mitotic stage, as well as the position of the centrosome using γ–tubulin antibodies. DPF3 showed a centrosomal localization in prophase. In pro-metaphase and metaphase, DPF3 signals were detectable at the centrosome and remained associated with

these structures throughout mitosis. At these stages, DPF3 also seems to be located to microtubules. Remarkably, DPF3 staining clearly appeared in the spindle midzone in anaphase and was also found at the midbodies during late telophase/cytokinesis (**Fig. 2**).

The spindle midzone plays a crucial role in regulating the completion of mitosis. To better characterize the localization of DPF3 in this multifunctional spindle midzone during anaphase, co-stainings were performed to more precisely detect CENP-E – a kinetochore-associated kinesin-like motor protein (Ciossani et al., 2018), Aurora B and MKLP2/KIF20A – two subunits of chromosomal passenger complex (CPC) (Carmena et al., 2012) (Serena et al., 2020) and PRC1 – a component of the bridging fibers which are non-kinetochore microtubule structures that connect sister K-fibers and balance the tension on kinetochores (Conkar et al., 2019) (Kajtez et al., 2016) (Jagrić et al., 2021)(Vukušić et al., 2017). In metaphase, a faint DPF3 signal was readily evident at the kinetochore where is slightly superimposed to that of CENP-E. At this stage, not all kinetochores that were occupied by CENP-E were found to contain DPF3 as the staining intensity of DPF3 varied amongst the kinetochores that displayed CENP-E staining. During early anaphase, DPF3 and CENP-E still remain co-localized at kinetochores, although DPF3 localized to portions of the spindle midzone that did not overlap with CENP-E. By mid-anaphase, co-localization between DPF3 and CENP-E in the central spindle zone is more prominent. At this stage, we remarkably observed a perfect co-localization with Aurora B and MKLP2/KIF20A as well as a partial overlap with the microtubule cross-linker PRC1 (**Fig. 3A**)**.** In late anaphase, when PRC1 is actively involved in midzone organization (Vukušić et al., 2021), a perfect co-localization was observed. These observations suggest that DPF3 might be part of the CPC molecular complex which overlaps bridging fibers structures during anaphase.

To identify potential interactions between DPF3 and CPC components such as Aurora B or PLK1 (Lee et al., 2021a) (Chu et al., 2011)**,** GST pull-down experiments were performed. Incubation of protein extracts from U2OS cells expressing FLAG-PLK1 or HA-Aurora B constructs with GST alone, GST-DPF3a or GFST-DPF3b followed by western blotting analysis revealed positive interaction with both DPF3a and DPF3b isoforms, while Myc-KIF2B or endogenous α-tubulin were not pulled-down (**Fig. 3B**).

Moreover, because DPF3 was located in microtubules-enriched structures such as bridging fibers, we checked if purified recombinant GST-DPF3a and/or GST-DPF3b might directly interact with microtubules. Using a microtubule co-sedimentation assay, we found that a significant amount of purified GST-DPF3a, and to a lesser extent GST-DPF3b, was pelleted down with taxol-stabilized microtubules, whereas without microtubules both DPF3a and DPF3b remained in the supernatant fraction (**Figs. S3A, S3B**). As shown in **Fig. 3B**, we found by GST pull-down assay that neither DPF3a nor DPF3b was able to interact with α-tubulin, suggesting that DPF3a and DPF3b preferentially interact with microtubules over free α-tubulin monomer.

Finally, we also detected DPF3 in the central region of the cytoplasmic bridge - the midbody - during late telophase and cytokinesis, although a weak staining still remained at the centrosomes. To more precisely identify the localization of DPF3 in the midbody compartments, co-immunofluorescence with antibodies against KIF4A (marker of midbody core), Citron Kinase (CT-K – marker of midbody ring) or MKPL2/KIF20A (marker of midbody arms) was performed. DPF3 was mainly detected with both KIF4A and CT-K proteins, suggesting that DPF3 is a component of the Flemming body, composed of the midbody ring and midbody core (**Fig. 3C).**

Altogether these results showed that DPF3 is not only located in the centrosome throughout mitosis but also appears in the spindle midzone/bridging fiber area during anaphase and finally concentrates in the midbody in cytokinesis.

DPF3 depletion induces G2/M blocking and apoptotic cell death

DPF3 was located in key mitotic structures including centrosome, spindle midzone/bridging fiber area and midbodies. Because such structures are important for orchestrating mitotic cell division, we assessed the impact of DPF3 knockdown on cell cycle. Transfection with the two different siRNAs against DPF3a and DPF3b in asynchronous U2OS cells caused a dramatic increase in the G2/M cell population compared with cells transfected with irrelevant Gl3 siRNA (siCtrl) (**Fig. 4A**). Interestingly, specific siRNA depletion of Brm and Brg1 did not block cells in G2/M (**Fig. S4A, S4B**) in agreement with previous publication (Giles et al., 2021). Increased histone H3 phosphorylation on Serine 10, a late G2/M marker, was also observed in total protein extracts of DPF3-depleted cells, supporting that cells accumulate in G2/M phase. In addition, higher expression of cyclin B1 was also

observed in protein extracts from DPF3-depleted cells (**Fig. 4B)**, indicating an unsatisfied spindle assembly checkpoint (SAC). We tested the possibility that the G2/M blocking of DPF3-depleted cells could be rescued by overexpressing exogenous DPF3. Unfortunately, overexpression of specific DPF3a and DPF3b in U2OS cell line triggers the formation and accumulation of protein like-aggregates (**Fig. S4C**). Because maintenance of protein solubility is a fundamental aspect of cellular homeostasis, DPF3 aggregation cannot lead us to properly conclude about the effect of DPF3 re-expression

To confirm that DPF3-depleted cells were arrested in M phase, we blocked control or DPF3-depleted U2OS cells at early mitosis using nocodazole and then released them into fresh medium. We found that 60% of DPF3-depleted cells were still in the mitotic phase 3 hours after release while more than 50% of control cells were already capable of exiting mitosis (**Figs. 4C, 4D**). To firmly validate that cell cycle blocking occurs in M phase, we analyzed cell cycle progression after release from the early S phase block by aphidicolin treatment (often termed G1/S synchrony). FACS analysis showed that a large population of both control and DPF3-depleted cells reached G2/M phase 8 hours after release from the aphidicolin block. Control cells could then further progress in the cell cycle and accumulated in the next G1 phase 16 hours after the release from aphidicolin block. In contrast, DPF3-depleted cells were were still detected in G2/M phase 16 hours after early S phase release (**Fig. 4E**). In parallel of FACS analysis, proteins were also extracted from DPF3-depleted cells at the indicated time intervals and were afterwards analyzed by western blotting using anti-phospho Serine 10 histone H3 antibodies. An increase of phosphorylated histone H3 on Serine 10 was observed 8 h after release from the aphidicolin block. The levels decreased 12 and 16 h after release (**Fig. 4F**), when control cells start to leave G2 phase and mitosis and accumulate in the next G1 phase. In contrast, the level remained high in DPF3-depleted cells at the same time intervals, indicating that those cells are still blocked in G2/M phase.

Because aphidicolin can induce DNA damages and activates a G2-checkpoint response (Arlt et al., 2004) (Sánchez-Molina et al., 2011), it is therefore possible that DPF3-depleted cells can not progress to mitosis due to G2 blocking. We have performed another cell cycle analysis using the validated inhibitor of CDK4/cyclin D1-CAS 546102-60-7 that induces G1 cell cycle arrest (Zhu et al., 2003). FACS analysis showed that control cells can normally progress in the cell cycle 24 hours after the

G1 block induced by CDK4 inhibitor, and accumulated in the next phase. However, a significant number of DPF3-depleted cells are still detected in G2/M phase 24 hours after the G1 release as similarly observed with aphidicolin (**Fig 4G**).

As prolonged mitotic arrest may eventually result in cell death, we also assessed the induction of apoptosis upon DPF3 depletion. Annexin V/PI staining experiment clearly showed a higher proportion of apoptotic cells upon DPF3 depletion compared to control cells (**Fig. 4H**). Cell cycle blockage and apoptosis induction upon DPF3 depletion translated into a significant decrease in cell number *in vitro* (**Fig. 4I**). Finally, live-cell imaging observations (**Movies 1-2**) are in full agreement with these data and clearly demonstrated that DPF3 depletion results in mitotic blocking followed by cell death.

DPF3 depletion induces chromosome oscillation, chromosome misalignment and prolonged mitosis

To further understand the cause of the mitotic blockage observed in DPF3-depleted cells, we performed fluorescent live-cell imaging experiments using U2OS expressing H2B-RFP/α-actin-GFP. Control cells showed a proper mitotic division (**Movie 3**). In contrast, we observed that DPF3-depleted cells exhibited chromosome hyper-oscillations and spent an unusually long time in mitosis (**Movies 4-5 and Fig. 5A**). Indeed, live-cell imaging revealed that DPF3-depleted cells were delayed in mitosis (DPF3 siRNA#1: 180 min as compared to Ctrl siRNA: 60 min) **(Fig. 5B)**. After a delay at metaphase, a proportion of DPF3-depleted cells did undergo anaphase and subsequent cytokinesis, leading to asynchronous/unscheduled chromatid separation as well as formation of nuclei with irregular shapes (formation of bi/multi-lobed nuclei) (**Movies 6-7**). Furthermore, we frequently observed induction of post-mitotic apoptotic cell death upon DPF3 depletion (**Movie 8 and Movie 2**), which is indicative of genomic instability.

To better assess the type of mitotic profile defects upon DPF3 depletion, we fixed cells and determined the percentage of cells with aberrant mitotic profiles including mis-aligned chromosomes, unaligned spindles, mono- or multi-polar spindles. Most of control cells (>75%) showed normal metaphases. Consistent with the hyper-oscillating chromosomes, DPF3 depletion induced a significant proportion of cells (around 50%) harboring chromosome misalignment (**Fig. 5C**).

To further validate the impact of DPF3 depletion on chromosome alignment, we treated cells with the Eg5 inhibitor monastrol and then monitored the restoration of KT–MT attachments during spindle bipolarization in response to drug washout. When released in medium containing MG132, control cells established bipolar spindles, and most chromosomes aligned correctly with less than 10% of these cells undergoing subsequent mitotic defects. In contrast, numerous chromosomes remained unaligned, and syntelic KT–MT attachment was clearly observed in more than 50% of DPF3-depleted cells (**Figs. 5D, 5E**). To further image the unaligned position of chromosomes at the metaphase plate, we took images of metaphase plates that were horizontally oriented in respect to the imaging plane (maximum intensity projections of z-stack scan). We measured the distance of the furthest DAPI-stained chromosomes in length and width at the metaphase plate and then determined the ratio. This quantification analysis revealed that the ratio was significantly higher (30%) in DPF3-depleted cells than in control cells, suggesting that chromosomes were more dispersed at the metaphase plate upon DPF3 depletion (**Fig. 5F**). Altogether, these results demonstrate that DPF3 depletion induced chromosome misalignment.

DPF3 depletion alters K-fiber stability and the establishment of stable kinetochore (KT)-microtubule (MT) attachments

Chromosome hyper-oscillations and failure in chromosome congression upon DPF3 depletion could arise from the destabilization of MTs and/or loss of © attachments. To evaluate the effect of DPF3 depletion on stable end-on KT–MT attachment, we performed a functional assay termed cold-stability assay. Unstable or weakened KT–MT attachments are disassembled when subjected to low temperature for a short time period, while stable and robust attachments are resistant to this condition. Control and DPF3-depleted U2OS cells were stained with anti-α-tubulin (K-fibers marker) and CREST (kinetochore marker) antibodies. In control cells, K-fibers were stable because they were well defined and bright. On the contrary, K-fibers in DPF3-depleted cells were wavy, discontinuous and exhibited a low density of α-tubulin staining, indicating a loss of K-fiber stability (**Fig. 6A**). To further quantify unstable K-fibers, we measured α-tubulin fluorescence (maximum intensity projections of z-stack scan) (Zhou et al., 2019a) (Warren et al., 2020) (Batman et al., 2022). DPF3 depletion resulted in a 40% decrease in α-tubulin fluorescence intensity

compared to control cells (**Fig. 6B**). Western blot analyses of lysates prepared from control and DPF3-depleted cells showed that the intensity changes in spindle MTs were not due to altered cellular abundance of α-tubulin (**Fig. 6C**). In DPF3-depleted cells, we frequently observed fewer cold-resistant K-fibers and several less stable and robust KT–MT attachments, inducing mal-oriented chromosomes (**Fig. 6A, white arrowheads and Fig. 6D**). Collectively, these results demonstrate that DPF3 depletion alters K-fiber stability and weakens KT–MT attachment; thereby compromising chromosome movement and alignment, which therefore result to the aforementioned mitotic defect phenotype.

DPF3 is a centriolar satellite protein involved in primary ciliogenesis and localizes at the apical surface in multiciliated cells

Many proteins associated with centriolar satellites are involved in the formation and function of the primary cilium. To investigate whether DPF3 was also located in centriolar satellite during ciliogenesis, we performed DPF3 staining in hTERT-RPE-1 cells grown in serum-deprived conditions to assemble primary cilia. In ciliated hTERT-RPE-1 cells visualized with anti-acetylated tubulin, DPF3 staining was detected in granular structures and showed a similar staining profile than PCM1, suggesting that DPF3 localizes to centriolar satellites (**Fig. 7A**). To determine whether DPF3 depletion resulted in a defect in primary cilium formation, we transfected hTERT-RPE-1 cells with DPF3 siRNAs, and cultured them in serum-free conditions to induce cilia formation. FACS analysis was first performed to validate that both control and DPF3-depleted cells were arrested in G0/G1 phase of the cell cycle when cilia formation occurs (**Fig. S5**). Under these conditions, we found that a large majority of DPF3-depleted cells (91% and 82% for siDPF3#1 and siDPF3#2, respectively) showed a lack of acetylated α-tubulin signal in the axoneme (**Fig. 7B, top panel and Fig. 7C**). IFT88 staining along the ciliary axoneme was also dramatically decreased upon DPF3 depletion, whereas it was still detected at mother centriole/basal body compartment (**Fig. 7B, bottom panel**). Together these data provide evidence that the axoneme extension is impaired upon DPF3 depletion. Interestingly, the dispersion and distribution of PCM1 granules in DPF3-depleted hTERT-RPE-1 cells was changed (**Figs. 7D, 7E, 7F**). Centriolar satellite dispersion was not caused by a change in PCM1 protein expression level (**Fig. 7G**), indicating that centriolar satellites remain intact upon DPF3 depletion. Together, these data

suggest that the inability of DPF3-depleted cells to ciliate is probably related to defective centriolar satellite organization/distribution around the centrosome rather the assembly *per se*. To better understand how DPF3 depletion impairs ciliogenesis, we examined centrioles and ciliary structures of serum-starved hTERT-RPE-1 cells depleted for DPF3 by transmission electron microscopy (TEM). Ciliogenesis is multistep process that begins with the docking of small Golgi-derived ciliary to the distal appendages of mother centrioles leading to the formation of distal appendage vesicles (DAVs). Small DAVs fused together and form larger primary ciliary vesicles followed by the formation and extension of ciliary axoneme. Control cells displayed mother centrioles associated with the ciliary pockets with extented axonemal shafts (**Figs. 7H, 7I**). In DPF3-depleted cells (which represents around 90% of cells - *see* Fig.7B; siDPF3 #1), the elongated ciliary axoneme was clearly absent. Interestingly, the docking of small ciliary vesicles to mother centrioles seems to be affected upon DPF3 depletion. Docking of the mother centriole to the pre-ciliary vesicles, and the initiation of axoneme extension required centriolar satellites(Hall et al., 2023b). We can therefore hypothesize that DPF3-depleted cells displayed reduced docking of the mother centriole to the ciliary vesicle and axoneme extension, probably due to destabilization/reorganization of centriolar satellites.

Discussion

In our previous understanding, DPF3 was recognized solely as a subunit of the BAF complex, existing in two isoforms. The established function of the isoform DPF3b consists in the binding to acetylated and/or methylated histones, therefore allowing the recruitment of the BAF complex to specific genomic regions during development. As for DPF3b, DPF3a isoform can bind the BAF complex but mainly through bridge protein like HRP2. So far, both isoforms have therefore been considered as regulators of gene expression.

Here we provide new evidences that DPF3 accumulates at different mitotic structures during mitosis including centrosomal compartment, spindle midzone/bridging fiber area and midbodies. DPF3 depletion triggers aberrant outcomes of mitosis and apoptosis, thus causing genomic instability (**Fig 8A**). This unexpected localization of DPF3 in mitotic structures classifies DPF3 as a new moonlighting protein playing an important role in mitosis and completes the repertoire

of chromatin-associated proteins such as ISWI, CHD4, INO80 ATPase, NuSAP or subunits of SRCAP and p400/Tip60 chromatin remodeling complexes that moonlight as mitotic regulators (Yokoyama et al., 2009) (Yokoyama et al., 2013) (Raemaekers et al., 2003) (Hur et al., 2010) (Chambers et al., 2012) (Messina et al., 2022). Different considerations support the hypothesis that DPF3-dependent mitotic phenotype is due to its direct (moonlighting) role rather than to an indirect effect on transcription of genes encoding mitotic proteins. First, mitotic alterations such as K-fiber instability, chromosome misalignment or multi-lobed cells are consistent with the localization of DPF3 to the mitotic apparatus and are frequently observed after the knockdown of multiple mitotic regulators (Zhou et al., 2019b) (Wei et al., 2011) (Bendre et al., 2016). Secondly, the absence of interaction for DPF3 with the core ATPase BAF subunits - Brg1 and Brm - as well as the lack of G2/M blocking upon Brg1 or Brm depletion suggest that DPF3 exerts its mitotic function in a Brg1/Brm-independent manner. Moreover, the dissociation of Brm and Brg1 from mitotic chromatin without any direct function in spindle assembly or maintenance as evidenced in the literature (Muchardt et al., 1996) strengths our hypothesis that DPF3 acts in a BAF-independent manner during mitosis.

From a mechanistic point of view, we observed that DPF3 is involved in K-fiber stability and correct chromosome positioning in metaphase. Metaphase plate seems to form correctly upon DPF3 depletion. However, we observed alignments with hyper-oscillating chromosomes. Consistent with the hyper-oscillating chromosomes, DPF3 depletion induced an increased fraction of cells harboring chromosome misalignment. One consequence of hyper-oscillating chromosomes in DPF3-depleted cells is that they have a propensity to lose their attachment to the mitotic spindle and activate the spindle assembly checkpoint, thus explaining the mitotic delays. Similar observations have been reported in the context of SF3B1 mutation (Cusan et al., 2023) or upon KIF18A depletion (Janssen et al., 2018), a mitotic kinesin which is also found within the bridging fiber (Jagrić et al., 2021).

During mitosis, the Chromosomal Passenger Complex (CPC) – a multiprotein complex composed of an enzymatic component Aurora B along with numerous regulatory proteins – dynamically localizes to different subcellular locations. It is located to the inner centromere region in metaphase and it moves to the central spindle microtubules during anaphase. Interaction and co-localization data support evidences that DPF3 might be a regulator of CPC localization and activity during

metaphase to anaphase transition. Interactions between CPC and both the chromatin and microtubules ensure that chromosomes are properly connected to microtubules from opposite poles of the mitotic spindle. The dual chromatin – microtubule interactions of CPC might, at least in part, depend on structural features of DPF3. Inner centromeric chromatin is enriched in epigenetic mark such as the dimethylated Lysine 4 on histone 3 (H3K4me2) (Sullivan and Karpen, 2004). Interestingly, this histone modification pattern can be read and bound by the double PHD finger of DPF3b (Lange et al., 2008), suggesting that DPF3b could act as a ‘‘reader’’ of the centromere epigenetic code to recruit CPC complex. The temporal regulation of CPC localization to the inner centromere is controlled by a TIP60-dependent acetylation of H3K4 (Niedzialkowska et al., 2022), an epigenetic mark also recognized by DPF3b (Lange et al., 2008). Deciphering the repertoire of histone post-translational modifications (HPTMs) that influence the recruitment of DPF3 to chromosomes to regulate the formation of the CPC deserves detailed investigations. In addition to its histone reader function, we hypothesize that DPF3 might recruit or correctly position the CPC to microtubule lattice via its microtubule binding capacity. Indeed, we provide in this study new experimental evidences that DPF3a, and to a lesser extent DPF3b, has the ability to recognize polymerized microtubules.

Kinetochores and CPC are considered as biomolecular condensates that are formed by liquid – liquid phase separation (Liu et al., 2020a) (Trivedi and Stukenberg, 2020)(Niedzialkowska et al., 2024). LLPS is often mediated by intrinsically disordered proteins (IDPs). These IDPs are characterized by a lack of stable secondary and tertiary structures and possess high conformational flexibility. Due to their flexible structure, IDPs are able to interact specifically but transiently/weakly with multiple protein partners, hence acting as “hubs” in protein-protein interaction (PPI) networks that drive the formation of biocondensate. Using *in silico* predictions and experimental evidences, we have recently demonstrated that both DPF3a and DPF3b isoforms contain intrinsically disordered regions (IDRs) (Mignon et al., 2021)(Mignon et al., 2022). Through their IDRs, DPF3a and DPF3b would be able to dynamically interact with multiple protein partners; driving the formation of a large protein structure connecting centromere/kinetochore and CPC to the microtubule lattice.

The multiple and dynamic PPI implicated in the assembly of huge protein complexes can be made possible and fine-tuned regulated by various post-

translational modifications (PTMs) on IDPs such as phosphorylation**.** A study published by Schick *et al*. reported an uncharacterized interaction between DPF3 and PLK1 (Schick et al., 2019), a crucial kinase being required for diverse mitotic functions (Combes et al., 2017). Remarkably, we also found that DPF3 and PLK1 are present in the same complex. Several studies demonstrated that accumulation of proteins such as MyoGEF (Asiedu et al., 2008), CLASP2 (Maia et al., 2012) or CEP55 (Fabbro et al., 2005) at the mitotic apparatus relies on phosphorylation by PLK1. As a model, we can therefore propose that a PLK1-dependent phosphorylation of DPF3 might be important not only for its correct localization to mitotic structures but also for its interaction with different mitotic partners. Conversely, it is also described that the correct localization of PLK1 in mitotic structures as well as its kinase activity is tightly regulated. Various mitotic proteins and chromatin remodelers such as CLIP-170, NCAPG2, NudC or RSF1 (Amin et al., 2014) (Kim et al., 2014) (Nishino et al., 2006) (Lee et al., 2021b) are involved in the tethering of active PLK1 to mitotic structures. At centromeres, PLK1 phosphorylates Borealin and Survivin in the CPC and this step is important for Aurora B docking (Lee et al., 2021a) and activities such as the phosphorylation of BubR1 or CENP-E (Ditchfield et al., 2003) (Kim et al., 2010). In this respect, we could also propose an alternative model according to DPF3 would act as a recruiter and spatial regulator of PLK1, thus playing the role of a bridge-protein for the interaction between PLK1 and CPC. Regardless of the molecular mechanism a better characterization of the DPF3 – PLK1 – Aurora B interaction could provide important molecular insights into the regulation of mitosis.

One key observation in our study is the localization of DPF3 in centriolar satellites in interphase. Despite disappearance of centriolar satellites during mitosis (Kubo et al., 1999), DPF3 remains at centrosomal position as similarly observed for other centriolar satellite protein such as OFD1 or CEP290 (Lopes et al., 2011). The observation that DPF3 is still present at centrosome during mitosis suggests an as-yet-unidentified role in this compartment. K-fiber plus-end dynamics is set by kinetochores themselves, although it can be also influenced by centrosomes (Dudka et al., 2019). The localization of DPF3 at the two attachments sites during mitosis – centrosome and spindle midzone – suggests that DPF3 may exert a tethering function between microtubule ends and either centrosomal proteins or /kinetochore proteins. A similar role and function have been attributed to the CEP57 protein which

is present at the attachment interfaces on both ends of mitotic microtubules (Emanuele and Stukenberg, 2007).

Because centriolar satellites are required for efficient ciliogenesis, it is not surprising that DPF3 also plays a crucial role in primary cilia formation in addition to its function in mitosis. In a model of primary ciliogenesis, we observed that DPF3 localizes in centriolar satellites that cluster at the basis of the centrosome/cilium complex. More importantly, we demonstrated that DPF3 knockdown disrupts the organization/distribution of centriolar satellites and blocks axoneme extension *in vitro* (**Fig. 8B**). Similar observations have been reported for centrosome-related proteins, such as LRRC45 or MARK4, which participate in ciliogenesis through axoneme extension (Kurtulmus et al., 2018)(Kuhns et al., 2013).

Centriolar satellites as well as centrosomes or pericentriolar matrix are also membrane-less organelles (MLOs) that are formed by LLPS phenomenon (Zhao et al., 2021) (Woodruff et al., 2017) (Jiang et al., 2021) (Raff, 2019) (Liu et al., 2020b). IDPs are also crucial components of these organelles and determine their respective activities. Dispersion of centriolar satellites upon DPF3 depletion therefore suggests that DPF3 might be a key IDP protein driving the homeostasis of these membrane-less granules by interacting with multiple partners. An interactomic profiling will certainly help to identify centriolar satellite partners. Although the precise molecular function of DPF3 in cilia should be further addressed, our study opens a new avenue of interpretation for previous published functions of DPF3. Lange *et al.* suggested that abnormal cardiac looping mediated by DPF3 knockdown was caused by a BAF-dependent transcriptional deregulation of genes coding for heart proteins (Lange et al., 2008). Because disturbed heart looping is frequently associated with primary cilia dysfunction (Klena et al., 2017)(Gabriel et al., 2021) it is possible that centriolar satellites-associated localization of DPF3 might be crucial for assembly and function of cilia in developmental heart tissues. Moreover, it is becoming more and more evident that mutations in centriolar satellite proteins such as CEP290 or OFD1 can cause defects in ciliogenesis (Papon et al., 2010) (Hannah et al., 2019). Whether deregulation of DPF3 is associated with ciliopathies really deserves to be further explored. Indeed, single nucleotide polymorphism (SNP) or over/down-expression of DPF3 has been already reported in ciliopathy-related diseases such as Tetralogy of Fallot (TOF) (Kaynak et al., 2003)(Lange et al., 2008), craniofacial ciliopathies (Vieira et al., 2008) (Brugmann et al., 2010), Hirschsprung's disease (Liu et al., 2014) (de

Pontual et al., 2007) or glioblastoma (Hiramatsu et al., 2017) (Yang et al., 2013) (Hoang-Minh et al., 2018) (Sarkisian and Semple-Rowland, 2019) (Goranci-Buzhala et al., 2021). Interestingly, studies demonstrated that centriolar satellite proteins, such CEP131 or CCDC113, are required for sperm motility by regulating protein trafficking in sperm cells (Hall et al., 2013) (Firat-Karalar et al., 2014). Mutation in CEP135 centriolar satellite protein leads to the formation of aggregates in flagella and induces multiple morphological abnormalities of the sperm flagella (MMAF), a rare disease associated with primary infertility (Sha et al., 2017). Interestingly, several clinical studies revealed that SNP in DPF3 was highly correlated with low sperm count accounting for motility defects and male infertility (Kosova et al., 2014) (SY et al., 2017) (Sato et al., 2018). In addition, we have recently demonstrated that both DPF3a and DPF3b isoforms tend to spontaneously aggregate *in vitro* (Mignon et al., 2021) (Mignon et al., 2022)(Leyder et al., 2022). Whether mutations in DPF3 would accelerate its aggregation, potentially affecting the normal function of spermatozoids and consequently leading to male infertility should be further investigated.

In conclusion, our study reveals a moonlighting localization and function of the DFP3 protein during mitosis and ciliogenesis, supporting a previously unknown role in human development and diseases such as cancers and ciliopathies.

Materials and Methods

Cell Culture, synchronization and treatment

U2OS cells were maintained in McCoy's 5A Medium. HeLa, HCT116, A549, MDA-MB-231 cancer cell lines and hTERT-RPE-1 cells were maintained in Dulbecco's Modified Eagle's Medium (DMEM - Lonza). All media were supplemented with 10% heat-inactivated fetal bovine serum (FBS), and cells were incubated at 37°C in the presence of 5% CO_2. KE37 cells were cultured in Roswell Park Memorial Institute medium (RPMI 1640, Lonza) supplemented with 7% FBS. All cell lines were from ATCC. Each cell line was routinely examined by microscope to check shape, growth conditions, proliferation and the presence of any contaminants. All cells were routinely (every two weeks) examined for mycoplasma contamination using MycoAlertTM Mycoplasma Detection Kit (Lonza, #LT07-118). Aphidicolin (#A0781), Nocodazole (#M1404), RO-3306 (#SML0569) and Monastrol drugs (#M8515) were from Sigma–

Aldrich. MG132 is from Med Chem Express (#HY-13259). CDK4/cyclin D1 - CAS 546102-60-7 inhibitor is from Calbiochem (#219476).

siRNA transfection

siRNAs were synthesized by Eurogentec and were used at a final concentration of 40 nM. Cells were plated 24 hours before transfection and then transfected at a confluence of approximately 50% using the calcium phosphate method. Mock-transfected cells (No si) and cells transfected with an irrelevant siRNA targeting Gl3 luciferase (siCtr) were used as negative controls. Two different siRNAs targeting DPF3 were used unless indicated. The sequences of the siRNAs used in this study are listed in **Table 1.**

Plasmids and Plasmid DNA transfection

Transient plasmid DNA transfection was carried out using Lipofectamine 2000 transfection reagent (Thermofisher, #11668030) according to manufacturer's instructions. Plasmids encoding DPF3a and DPF3b cDNA in fusion with GST epitope were generated by e-Zyvec. pCMV3-KIF2B-Myc and pCMV3-hAURKB-HA are from Sino Biological Inc. pTXB3-Flag PLK1 was a gift from Stefano Ferrari (Addgene plasmid # 68271, RRID: Addgene 68271).

RT-qPCR

Total RNA was extracted using the NucleoSpin RNA kit (Macherey-Nagel, #740955) and measured by Nanodrop. Reverse transcription was performed with the RevertAid H minus first strand cDNA synthesis kit (ThermoFisher Scientific, #K163) according to the manufacturer's instructions. Quantitative PCR was performed with a LightCycler 480 instrument (Roche, #04707516001) with β-actin as control. All measurements were realized in triplicate. Primer sequences are available in **Table 2**.

Total protein extraction

For total protein extraction, adherent and floating cells were collected and lysed with a lysis buffer containing 1% SDS, 40 mM Tris-HCl (pH 7.5), 1 mM EDTA, complete EDTA-free protease inhibitor (Sigma-Aldrich, #11697498001) and phosphatase inhibitor (Sigma-Aldrich, #0490684500).

Isolation of cytoplasmic, nucleoplasm and chromatin-enriched fractions

Chromatin fractionation was carried out as previously described. Three different fractions were collected: cytoplasmic fraction (CF); nuclear soluble fraction (NSF), chromatin-enriched fraction (CEF). MEK2 and Lamin A/C proteins were used as a fractionation control for cytoplasmic fraction (CF) and chromatin-enriched fraction (CEF), respectively.

Purification of centrosomes from mammalian cells

Isolation and purification of centrosome from KE37 cells was performed according to the procedure described by (Gogendeau et al., 2015).

Western blotting (WB) analysis

Proteins were quantified with the BCA protein assay kit (Pierce, #23225) and separated by SDS-PAGE to be transferred onto a PVDF (polyvinylidene fluoride) membrane. After blocking of non-specific binding sites, proteins were detected with primary antibody (**Table 3**) and HRP-conjugated secondary antibody. Finally, membranes were developed using chemiluminescence detection. HSC70, HSP90 or β–actin antibody was used as loading control. BlueEasy Prestained Protein Marker (Nippon Genetics) was used as the molecular weight ladder.

Co-immunoprecipitation (Co-IP) analysis

U2OS cells were washed with ice-cold PBS, lysed with lysis buffer (20 mM Tris-HCl pH 7.5, 150 mM NaCl, 5 mM EDTA, 5mM EGTA, 1% Triton X-100, complete EDTA-free protease inhibitor (Sigma-Aldrich, #11697498001) and phosphatase inhibitor (Sigma-Aldrich, #04906845001). Collected cells were sonicated and then incubated on ice for 30 min. The supernatant was clarified by centrifugation at 5000 g for 10 min at 4°C. After quantification, protein extracts were diluted to equal concentrations and then pre-cleared with protein A/G agarose beads (Santa Cruz Biotechnology, #sc-2003). After centrifugation at 5000 x g for 5 min at 4 °C, the supernatants were incubated on the rotor overnight at 4 °C with the indicated antibodies (**Table 4**). IgGs of the corresponding species were used as negative controls. A/G beads were then added to the lysates for 2 hours at 4 °C. After centrifugation (600 x g for 10 min at 4 °C), beads were collected and washed 4 times with lysis buffer, resuspended in 2X Laemmli buffer, boiled for 10 min at 95 °C and centrifuged at 5000 x g for 5 min.

Purified proteins were resolved by SDS-PAGE and subjected to western blotting analysis.

Purification of GST fusion proteins

For GST fusion proteins, GST-DPF3a and GST-DPF3b were constructed into a pGEX-like vector by eZyvec and expressed in *E. coil* BL21 cells (Stratagene, #200131). Logarithmic phase BL21 cells were induced by IPTG (1 mM) and cultured overnight at 16 °C. Cells were harvested and then lysed in IPLS buffer (0.5% NP40, 50 mM Tris-HCl, 120 mM NaCl, 0.5 mM EDTA, pH 8 and 10% glycerol) 30 min at 4°C. Cell lysates were then subjected to centrifugation 10 min at 10 000 x g. Fusion proteins were purified by glutathione-conjugated sepharose 4B beads (GE Healthcare).

GST pull-down assay

Protein lysates from mock-or transfected U2OS cells lysate were incubated with GST recombinant proteins immobilized on glutathione-conjugated sepharose beads at 4°C for 2 h. Beads were extensively washed and eluted proteins run on SDS-PAGE were analyzed by Western blotting using indicated antibody.

Microtubule (MT) co-sedimentation assay

MT co-sedimentation assays were performed using the Microtubule Binding Protein Spin-down Assay Kit (Cytoskeleton, #BK029) as described by the manufacturer. Briefly, preparations of GST-DPF3a and GST-DPF3b were centrifuged at 100 000 x g for 30 min at 4°C to remove aggregates of insoluble material. The supernatants were incubated with 2 µM taxol-stabilized MTs prepared from 50 µM tubulin for 30 min at room temperature. The solutions were then subjected to centrifugation at 100 000 x g for 40 min at room temperature to pellet MTs with bound protein. After solubilization of the pellet fraction, equal volumes of the pellet and supernatant fractions were resolved by SDS-PAGE, followed by Coomassie blue staining.

Immunofluorescence

Cells were seeded on coverslips in 24-well plates. Cells were rinsed with PBS, permeabilized or not with ice-cold CSK buffer (300 mM sucrose, 3 mM $MgCl_2$, 10 mM PIPES pH 7.0, 100 mM NaCl, 0.25% Triton X-100) to remove soluble protein and then fixed with cold methanol/acetone in an 80/20 ratio for 10 min at -20 °C. After several

washes, the coverslips were blocked in PBS with 1% BSA (PBS-BSA) for 30 min at room temperature and incubated with primary antibodies (**Table 5**) diluted in PBS-BSA for 2 hours at room temperature. The coverslips were then washed and incubated with appropriate Alexa Fluor-conjugated secondary antibodies diluted in PBS-BSA for 1 hour at room temperature. Nuclear cells were counterstained with 1mg/mL DAPI (Life Technologies, #D1306) for 10 min at room temperature in the dark. The coverslips were mounted onto microscope slides and images were obtained with a Leica TCS SP5 laser scanning confocal microscope or Zeiss LSM 880 Airyscan 1 High Resolution microscope with a 63X/1.25NA objective which is in this case indicated in the legend.
To quantify PCM1 dispersion, a circle at the basis of cilia was drawn in control condition (No si). In DPF3-depleted cells, the circle was place in the area where the signal is still brightest. The pixel density of anti-PCM1 staining in corresponding area was measured using Image J software. Fluorescence intensity was quantified and signal level in control cells (No si) was normalized to 1.

Cold-stable microtubule assay

Briefly, U2OS cells were blocked in metaphase by treating them with RO3306 (9 μM - 45 min) followed by MG132 (10 μM - 30 min). Cells were then incubated in ice-cold Leibovitz L-15 medium (Thermofisher, Cat#21083) supplemented with 20 mM HEPES pH 7.0 for 10 min. Cells were fixed with paraformaldehyde 4% in 100 mM PIPES, 25 mM HEPES, 10 mM EGTA, 1 mM $MgCl_2$, and 0.2% Triton X-100. Immunofluorescence was done as described above. Images were captured using Zeiss LSM 880 Airyscan 1 High Resolution microscope with a 63X/1.25NA objective controlled by Zeiss Zen imaging software. Image J was used to quantify fluorescence intensities.

Live cell imaging

After transfection, U2OS cells were plated in a cell culture dish with two individual compartments. Live imaging for 24 hours at a time lapse of 5 min was performed with a Nikon A1R microscope. Image J was used for image analysis.

Transmission electron microscopy (TEM)

Cells grown on glass slides were fixed in a 1.6% glutaraldehyde solution in 0.1 M sodium phosphate buffer (pH 7.4) at room temperature and then stored at 4°C. After

three rinsing in 0.1 M cacodylate buffer pH 7.4 (15 min each), samples were postfixed in a 1 % osmium tetroxide and 1 % potassium ferrocyanide solution in 0.1 M cacodylate buffer for 1 hour at room temperature. Cells were subsequently rinsed in DDW and dehydrated in a series of ethanol baths (96 %, 100% three times, 15 min each) and then progressively embedded in Agar 100 resin (ethanol/resin 1:1, 100 % resin two times, 2 hours for each bath). Resin blocs were finally left to harden at 60 °C in an oven for 2 days. After removing the glass slides, ultrathin serial sections (70 nm) were obtained with a Reichert Ultracut S ultramicrotome equipped with a Diatome diamond knife and collected on copper slot grids with a formvar support film. Sections were stained with lead citrate and uranyl acetate. TEM observations were performed with a JEOL JEM-1400 transmission electron microscope, equipped with a Morada camera, at a 100 kV acceleration voltage.

Cell cycle analysis

Cells were trypsinized and washed 2 times with PBS 1X. They were then fixed with cold 70% ethanol and stored at -20°C until staining with propidium iodide (PI). Cells were centrifuged 5 min at 800 x g and washed 2 times with PBS 1X. Then, cells were resuspended in 300 µL of PI working solution (50 µg/mL of propidium iodide and 50 µg/mL of Rnase A in PBS) then incubated for 30 min in darkness and analyzed by flow cytometry using a FACS Calibur II Modfit Software Version 3.2.1, CellQuest Version 3.2. A total of 10,000 live, single cells were recorded for each sample. Total cells were first gated according to their intrinsic size (FSC) and granularity (SSC) properties on a log scale. The gate excluded cellular debris from living cells. Living cells were then gated based on the area (FL2-A) and the width (FL2-W) of the signal for DNA staining to exclude doublets.

Apoptosis analysis

Apoptosis was measured with the FITC-Annexin V apoptosis Detection Kit I (BD Biosciences, #556547) according to manufacturer's instructions. Flow cytometry was performed and data were analyzed with CellQuest software (BD Biosciences). Annexin V^+/PI^- and Annexin V^+/PI^+ cells were considered apoptotic.

Growth curve analysis

After transfection, U2OS cells were trypsinized and viable cells were plated at a density of 100,000 cells per well in a 6 well plate. Cell counting was carried out every 24 hours for 4 days, and the medium was replaced every 2 days.

Statistical analysis

Unless otherwise indicated, data are expressed as mean ± SD. Statistical tests used were indicated in each figure legend. p-values less than 0.05 were considered statistically significant. p-values (relative to siCtrl) are displayed as following: * $p < 0.05$; ** $p < 0.01$; *** $p < 0.001$, **** $p < 0.0001$. Exact p-values are indicated in each graph.

Acknowledgments

The authors thank the GIGA Cell Imaging and Flow Cytometry for technical assistance. We thank the scientific illustrator, Adeline Deward (Illumine), for designing and formatting figures. We also thank Anne Marie Tassin's Lab for their technical advices and scientific inputs. G.V. is a FNRS-TELEVIE fellow. J.M is an Aspirant FNRS fellow. S.H. is a FNRS Research Associate. C.M. and D.M. are FNRS Senior Research Associates. They all thank FNRS for financial support.

Competing interests

The authors declare that they have no competing interests. C.K. received consulting fees from Sanofi (international advisory board). The sponsors had no role in the design of the study, the collection and analysis of the data, or in the preparation of the manuscript.

Fundings

This work was supported by grants from the FNRS (Fonds National de la Recherche Scientifique) – Belgium, TELEVIE, Fonds Léon Frédéricq- Université de Liège and Fonds Spéciaux de la Recherche de l'Université de Liège (ULiege). CCMA electron microscopy equipment was funded by the Région Sud - Provence-Alpes-Côte d'Azur, the Conseil Général des Alpes Maritimes and the GIS-IBiSA. Work in Vernos lab was supported by grants from the Spanish Ministry of Economy BFU2015-68726-P, the

Ministry of Science, Innovation and Universities PGC2018-096976-B-I00 and AGAUR-SGR 478 from the Generalitat de Catalunya.

Author contributions

G.V, M.M., F.O., C.M., C.K., D.M. conceived and designed the experiments;
G.V., A.M.O, A.G., J.S., F.O., S.H., J.M., T.L., N.B., M.M. performed the experiments;
G.V., M.M., I.V., D.M. analyzed the data;
G.V., D.M. wrote the paper;
All authors have read and approved the manuscript for publication.

References

Amin, M. A., Itoh, G., Iemura, K., Ikeda, M. and Tanaka, K. (2014). CLIP-170 recruits PLK1 to kinetochores during early mitosis for chromosome alignment. *J Cell Sci* **127**, 2818–24.

Arlt, M. F., Xu, B., Durkin, S. G., Casper, A. M., Kastan, M. B. and Glover, T. W. (2004). BRCA1 Is Required for Common-Fragile-Site Stability via Its G_2/M Checkpoint Function. *Mol Cell Biol* **24**, 6701–6709.

Asiedu, M., Wu, D., Matsumura, F. and Wei, Q. (2008). Phosphorylation of MyoGEF on Thr-574 by Plk1 promotes MyoGEF localization to the central spindle. *J Biol Chem* **283**, 28392–400.

Batman, U., Deretic, J. and Firat-Karalar, E. N. (2022). The ciliopathy protein CCDC66 controls mitotic progression and cytokinesis by promoting microtubule nucleation and organization. *PLoS Biol* **20**, e3001708.

Baumann, K. (2012). Cell cycle: Order in the pericentriolar material.

Bendre, S., Rondelet, A., Hall, C., Schmidt, N., Lin, Y.-C., Brouhard, G. J. and Bird, A. W. (2016). GTSE1 tunes microtubule stability for chromosome alignment and segregation by inhibiting the microtubule depolymerase MCAK. *J Cell Biol* **215**, 631–647.

Brugmann, S. A., Cordero, D. R. and Helms, J. A. (2010). Craniofacial ciliopathies: A new classification for craniofacial disorders. *Am J Med Genet A* **152A**, 2995–3006.

Carmena, M., Wheelock, M., Funabiki, H. and Earnshaw, W. C. (2012). The chromosomal passenger complex (CPC): from easy rider to the godfather of mitosis. *Nat Rev Mol Cell Biol* **13**, 789–803.

Chambers, A. L., Ormerod, G., Durley, S. C., Sing, T. L., Brown, G. W., Kent, N. A. and Downs, J. A. (2012). The INO80 chromatin remodeling complex prevents polyploidy and maintains normal chromatin structure at centromeres. *Genes Dev* **26**, 2590–603.

Chu, Y., Yao, P. Y., Wang, W., Wang, D., Wang, Z., Zhang, L., Huang, Y., Ke, Y., Ding, X. and Yao, X. (2011). Aurora B kinase activation requires survivin priming phosphorylation by PLK1. *J Mol Cell Biol* **3**, 260–7.

Ciossani, G., Overlack, K., Petrovic, A., Huis In 't Veld, P. J., Koerner, C., Wohlgemuth, S., Maffini, S. and Musacchio, A. (2018). The kinetochore proteins CENP-E and CENP-F directly and specifically interact with distinct BUB mitotic checkpoint Ser/Thr kinases. *J Biol Chem* **293**, 10084–10101.

Combes, G., Alharbi, I., Braga, L. G. and Elowe, S. (2017). Playing polo during mitosis: PLK1 takes the lead. *Oncogene* **36**, 4819–4827.

Conkar, D., Bayraktar, H. and Firat-Karalar, E. N. (2019). Centrosomal and ciliary targeting of CCDC66 requires cooperative action of centriolar satellites, microtubules and molecular motors. *Sci Rep* **9**, 14250.

Cui, H., Schlesinger, J., Schoenhals, S., Tönjes, M., Dunkel, I., Meierhofer, D., Cano, E., Schulz, K., Berger, M. F., Haack, T., et al. (2016). Phosphorylation of the chromatin remodeling factor DPF3a induces cardiac hypertrophy through releasing HEY repressors from DNA. *Nucleic Acids Res* **44**, 2538–53.

Cusan, M., Shen, H., Zhang, B., Liao, A., Yang, L., Jin, M., Fernandez, M., Iyer, P., Wu, Y., Hart, K., et al. (2023). SF3B1 mutation and ATM deletion codrive leukemogenesis via centromeric R-loop dysregulation. *J Clin Invest* **133**,.

de Pontual, L., Pelet, A., Clement-Ziza, M., Trochet, D., Antonarakis, S. E., Attie-Bitach, T., Beales, P. L., Blouin, J.-L., Dastot-Le Moal, F., Dollfus, H., et al. (2007). Epistatic interactions with a common hypomorphic RET allele in syndromic Hirschsprung disease. *Hum Mutat* **28**, 790–6.

Ditchfield, C., Johnson, V. L., Tighe, A., Ellston, R., Haworth, C., Johnson, T., Mortlock, A., Keen, N. and Taylor, S. S. (2003). Aurora B couples chromosome alignment with anaphase by targeting BubR1, Mad2, and Cenp-E to kinetochores. *J Cell Biol* **161**, 267–80.

Dudka, D., Castrogiovanni, C., Liaudet, N., Vassal, H. and Meraldi, P. (2019). Spindle-Length-Dependent HURP Localization Allows Centrosomes to Control Kinetochore-Fiber Plus-End Dynamics. *Current Biology* **29**, 3563-3578.e6.

Emanuele, M. J. and Stukenberg, P. T. (2007). Xenopus Cep57 Is a Novel Kinetochore Component Involved in Microtubule Attachment. *Cell* **130**, 893–905.

Fabbro, M., Zhou, B.-B., Takahashi, M., Sarcevic, B., Lal, P., Graham, M. E., Gabrielli, B. G., Robinson, P. J., Nigg, E. A., Ono, Y., et al. (2005). Cdk1/Erk2- and Plk1-Dependent Phosphorylation of a Centrosome Protein, Cep55, Is Required for Its Recruitment to Midbody and Cytokinesis. *Dev Cell* **9**, 477–488.

Firat-Karalar, E. N., Sante, J., Elliott, S. and Stearns, T. (2014). Proteomic analysis of mammalian sperm cells identifies new components of the centrosome. *J Cell Sci* **127**, 4128–33.

Gabriel, G. C., Young, C. B. and Lo, C. W. (2021). Role of cilia in the pathogenesis of congenital heart disease. *Semin Cell Dev Biol* **110**, 2–10.

Giles, K. A., Gould, C. M., Achinger-Kawecka, J., Page, S. G., Kafer, G. R., Rogers, S., Luu, P.-L., Cesare, A. J., Clark, S. J. and Taberlay, P. C. (2021). BRG1 knockdown inhibits proliferation through multiple cellular pathways in prostate cancer. *Clin Epigenetics* **13**, 37.

Gogendeau, D., Guichard, P. and Tassin, A.-M. (2015). Purification of centrosomes from mammalian cell lines. *Methods Cell Biol* **129**, 171–189.

Goranci-Buzhala, G., Mariappan, A., Ricci-Vitiani, L., Josipovic, N., Pacioni, S., Gottardo, M., Ptok, J., Schaal, H., Callaini, G., Rajalingam, K., et al. (2021). Cilium induction triggers differentiation of glioma stem cells. *Cell Rep* **36**, 109656.

Hall, E. A., Keighren, M., Ford, M. J., Davey, T., Jarman, A. P., Smith, L. B., Jackson, I. J. and Mill, P. (2013). Acute versus chronic loss of mammalian Azi1/Cep131 results in distinct ciliary phenotypes. *PLoS Genet* **9**, e1003928.

Hall, E. A., Kumar, D., Prosser, S. L., Yeyati, P. L., Herranz-Pérez, V., García-Verdugo, J. M., Rose, L., McKie, L., Dodd, D. O., Tennant, P. A., et al. (2023a). Centriolar satellites expedite mother centriole remodeling to promote ciliogenesis. *Elife* **12**,.

Hall, E. A., Kumar, D., Prosser, S. L., Yeyati, P. L., Herranz-Pérez, V., García-Verdugo, J. M., Rose, L., McKie, L., Dodd, D. O., Tennant, P. A., et al. (2023b). Centriolar satellites expedite mother centriole remodeling to promote ciliogenesis. *Elife* **12**,.

Hannah, W. B., DeBrosse, S., Kinghorn, B., Strausbaugh, S., Aitken, M. L., Rosenfeld, M., Wolf, W. E., Knowles, M. R. and Zariwala, M. A. (2019). The expanding phenotype of *OFD1* -related disorders: Hemizygous loss-of-function variants in three patients with primary ciliary dyskinesia. *Mol Genet Genomic Med* **7**, e911.

Hiramatsu, H., Kobayashi, K., Kobayashi, K., Haraguchi, T., Ino, Y., Todo, T. and Iba, H. (2017). The role of the SWI/SNF chromatin remodeling complex in maintaining the stemness of glioma initiating cells. *Sci Rep* **7**, 889.

Ho, L. and Crabtree, G. R. (2010). Chromatin remodelling during development. *Nature* **463**, 474–484.

Hoang-Minh, L. B., Dutra-Clarke, M., Breunig, J. J. and Sarkisian, M. R. (2018). Glioma cell proliferation is enhanced in the presence of tumor-derived cilia vesicles. *Cilia* **7**, 6.

Hur, S.-K., Park, E.-J., Han, J.-E., Kim, Y.-A., Kim, J.-D., Kang, D. and Kwon, J. (2010). Roles of human INO80 chromatin remodeling enzyme in DNA replication and chromosome segregation suppress genome instability. *Cellular and Molecular Life Sciences* **67**, 2283–2296.

Jagrić, M., Risteski, P., Martinčić, J., Milas, A. and Tolić, I. M. (2021). Optogenetic control of PRC1 reveals its role in chromosome alignment on the spindle by overlap length-dependent forces. *Elife* **10**,.

Janssen, L. M. E., Averink, T. V, Blomen, V. A., Brummelkamp, T. R., Medema, R. H. and Raaijmakers, J. A. (2018). Loss of Kif18A Results in Spindle Assembly Checkpoint Activation at Microtubule-Attached Kinetochores. *Curr Biol* **28**, 2685-2696.e4.

Jiang, X., Ho, D. B. T., Mahe, K., Mia, J., Sepulveda, G., Antkowiak, M., Jiang, L., Yamada, S. and Jao, L.-E. (2021). Condensation of pericentrin proteins in human cells illuminates phase separation in centrosome assembly. *J Cell Sci* **134**,.

Kadoch, C. and Crabtree, G. R. (2015). Mammalian SWI/SNF chromatin remodeling complexes and cancer: Mechanistic insights gained from human genomics. *Sci Adv* **1**, e1500447.

Kajtez, J., Solomatina, A., Novak, M., Polak, B., Vukušić, K., Rüdiger, J., Cojoc, G., Milas, A., Šumanovac Šestak, I., Risteski, P., et al. (2016). Overlap microtubules link sister k-fibres and balance the forces on bi-oriented kinetochores. *Nat Commun* **7**, 10298.

Kaynak, B., von Heydebreck, A., Mebus, S., Seelow, D., Hennig, S., Vogel, J., Sperling, H.-P., Pregla, R., Alexi-Meskishvili, V., Hetzer, R., et al. (2003). Genome-wide array analysis of normal and malformed human hearts. *Circulation* **107**, 2467–74.

Kim, Y., Holland, A. J., Lan, W. and Cleveland, D. W. (2010). Aurora kinases and protein phosphatase 1 mediate chromosome congression through regulation of CENP-E. *Cell* **142**, 444–55.

Kim, J. H., Shim, J., Ji, M.-J., Jung, Y., Bong, S. M., Jang, Y.-J., Yoon, E.-K., Lee, S.-J., Kim, K. G., Kim, Y. H., et al. (2014). The condensin component NCAPG2 regulates microtubule-kinetochore attachment through recruitment of Polo-like kinase 1 to kinetochores. *Nat Commun* **5**, 4588.

Klena, N. T., Gibbs, B. C. and Lo, C. W. (2017). Cilia and Ciliopathies in Congenital Heart Disease. *Cold Spring Harb Perspect Biol* **9**,.

Kosova, G., Hotaling, J. M., Ohlander, S., Niederberger, C., Prins, G. S. and Ober, C. (2014). Variants in DPF3 and DSCAML1 are associated with sperm morphology. *J Assist Reprod Genet* **31**, 131–7.

Kubo, A., Sasaki, H., Yuba-Kubo, A., Tsukita, S. and Shiina, N. (1999). Centriolar satellites: molecular characterization, ATP-dependent movement toward centrioles and possible involvement in ciliogenesis. *J Cell Biol* **147**, 969–80.

Kuhns, S., Schmidt, K. N., Reymann, J., Gilbert, D. F., Neuner, A., Hub, B., Carvalho, R., Wiedemann, P., Zentgraf, H., Erfle, H., et al. (2013). The microtubule affinity regulating kinase MARK4 promotes axoneme extension during early ciliogenesis. *Journal of Cell Biology* **200**, 505–522.

Kurtulmus, B., Yuan, C., Schuy, J., Neuner, A., Hata, S., Kalamakis, G., Martin-Villalba, A. and Pereira, G. (2018). LRRC45 contributes to early steps of axoneme extension. *J Cell Sci* **131**,.

Lange, M., Kaynak, B., Forster, U. B., Tönjes, M., Fischer, J. J., Grimm, C., Schlesinger, J., Just, S., Dunkel, I., Krueger, T., et al. (2008). Regulation of muscle development by DPF3, a novel histone acetylation and methylation reader of the BAF chromatin remodeling complex. *Genes Dev* **22**, 2370–84.

Lee, H.-S., Min, S., Jung, Y.-E., Chae, S., Heo, J., Lee, J.-H., Kim, T., Kang, H.-C., Nakanish, M., Cha, S.-S., et al. (2021a). Spatiotemporal coordination of the RSF1-PLK1-Aurora B cascade establishes mitotic signaling platforms. *Nat Commun* **12**, 5931.

Lee, H.-S., Min, S., Jung, Y.-E., Chae, S., Heo, J., Lee, J.-H., Kim, T., Kang, H.-C., Nakanish, M., Cha, S.-S., et al. (2021b). Spatiotemporal coordination of the RSF1-PLK1-Aurora B cascade establishes mitotic signaling platforms. *Nat Commun* **12**, 5931.

Lessard, J., Wu, J. I., Ranish, J. A., Wan, M., Winslow, M. M., Staahl, B. T., Wu, H., Aebersold, R., Graef, I. A. and Crabtree, G. R. (2007). An essential switch in subunit composition of a chromatin remodeling complex during neural development. *Neuron* **55**, 201–15.

Leyder, T., Mignon, J., Mottet, D. and Michaux, C. (2022). Unveiling the Metal-Dependent Aggregation Properties of the C-terminal Region of Amyloidogenic Intrinsically Disordered Protein Isoforms DPF3b and DPF3a. *Int J Mol Sci* **23**,.

Liu, H., Luo, Y., Li, S., Wang, S., Wang, N. and Jin, X. (2014). Expression profiles of HA117 and its neighboring gene DPF3 in different colon segments of Hirschsprung's disease. *Int J Clin Exp Pathol* **7**, 3966–74.

Liu, X., Liu, X., Wang, H., Dou, Z., Ruan, K., Hill, D. L., Li, L., Shi, Y. and Yao, X. (2020a). Phase separation drives decision making in cell division. *J Biol Chem* **295**, 13419–13431.

Liu, X., Liu, X., Wang, H., Dou, Z., Ruan, K., Hill, D. L., Li, L., Shi, Y. and Yao, X. (2020b). Phase separation drives decision making in cell division. *J Biol Chem* **295**, 13419–13431.

Lopes, C. A. M., Prosser, S. L., Romio, L., Hirst, R. A., O'Callaghan, C., Woolf, A. S. and Fry, A. M. (2011). Centriolar satellites are assembly points for proteins implicated in human ciliopathies, including oral-facial-digital syndrome 1. *J Cell Sci* **124**, 600–12.

Maia, A. R. R., Garcia, Z., Kabeche, L., Barisic, M., Maffini, S., Macedo-Ribeiro, S., Cheeseman, I. M., Compton, D. A., Kaverina, I. and Maiato, H. (2012). Cdk1 and Plk1 mediate a CLASP2 phospho-switch that stabilizes kinetochore–microtubule attachments. *Journal of Cell Biology* **199**, 285–301.

Messina, G., Prozzillo, Y., Monache, F. D., Santopietro, M. V. and Dimitri, P. (2022). Evolutionary conserved relocation of chromatin remodeling complexes to the mitotic apparatus. *BMC Biol* **20**, 172.

Mignon, J., Mottet, D., Verrillo, G., Matagne, A., Perpète, E. A. and Michaux, C. (2021). Revealing Intrinsic Disorder and Aggregation Properties of the DPF3a Zinc Finger Protein. *ACS Omega* **6**, 18793–18801.

Mignon, J., Mottet, D., Leyder, T., Uversky, V. N., Perpète, E. A. and Michaux, C. (2022). Structural characterisation of amyloidogenic intrinsically disordered zinc finger protein isoforms DPF3b and DPF3a. *Int J Biol Macromol* **218**, 57–71.

Muchardt, C., Reyes, J. C., Bourachot, B., Leguoy, E. and Yaniv, M. (1996). The hbrm and BRG-1 proteins, components of the human SNF/SWI complex, are phosphorylated and excluded from the condensed chromosomes during mitosis. *EMBO J* **15**, 3394–3402.

Niedzialkowska, E., Liu, L., Kuscu, C., Mayo, Z., Minor, W., Strahl, B. D., Adli, M. and Stukenberg, P. T. (2022). Tip60 acetylation of histone H3K4 temporally controls chromosome passenger complex localization. *Mol Biol Cell* **33**, br15.

Niedzialkowska, E., Truong, T. M., Eldredge, L. A., Ali, A., Redemann, S. and Stukenberg, P. T. (2024). Chromosomal passenger complex condensates generate parallel microtubule bundles in vitro. *Journal of Biological Chemistry* 105669.

Nishino, M., Kurasawa, Y., Evans, R., Lin, S.-H., Brinkley, B. R. and Yu-Lee, L.-Y. (2006). NudC is required for Plk1 targeting to the kinetochore and chromosome congression. *Curr Biol* **16**, 1414–21.

Papon, J. F., Perrault, I., Coste, A., Louis, B., Gérard, X., Hanein, S., Fares-Taie, L., Gerber, S., Defoort-Dhellemmes, S., Vojtek, A. M., et al. (2010). Abnormal respiratory cilia in non-syndromic Leber congenital amaurosis with CEP290 mutations. *J Med Genet* **47**, 829–34.

Raemaekers, T., Ribbeck, K., Beaudouin, J., Annaert, W., Van Camp, M., Stockmans, I., Smets, N., Bouillon, R., Ellenberg, J. and Carmeliet, G. (2003). NuSAP, a novel microtubule-associated protein involved in mitotic spindle organization. *Journal of Cell Biology* **162**, 1017–1029.

Raff, J. W. (2019). Phase Separation and the Centrosome: A Fait Accompli?

Salisbury, J. L., Suino, K. M., Busby, R. and Springett, M. (2002). Centrin-2 Is Required for Centriole Duplication in Mammalian Cells. *Current Biology* **12**, 1287–1292.

Sánchez-Molina, S., Mortusewicz, O., Bieber, B., Auer, S., Eckey, M., Leonhardt, H., Friedl, A. A. and Becker, P. B. (2011). Role for hACF1 in the G2/M damage checkpoint. *Nucleic Acids Res* **39**, 8445–8456.

Sarkisian, M. R. and Semple-Rowland, S. L. (2019). Emerging Roles of Primary Cilia in Glioma. *Front Cell Neurosci* **13**, 55.

Sato, Y., Hasegawa, C., Tajima, A., Nozawa, S., Yoshiike, M., Koh, E., Kanaya, J., Namiki, M., Matsumiya, K., Tsujimura, A., et al. (2018). Association of TUSC1 and DPF3 gene polymorphisms with male infertility. *J Assist Reprod Genet* **35**, 257–263.

Schick, S., Rendeiro, A. F., Runggatscher, K., Ringler, A., Boidol, B., Hinkel, M., Májek, P., Vulliard, L., Penz, T., Parapatics, K., et al. (2019). Systematic characterization of BAF mutations provides insights into intracomplex synthetic lethalities in human cancers. *Nat Genet* **51**, 1399–1410.

Serena, M., Bastos, R. N., Elliott, P. R. and Barr, F. A. (2020). Molecular basis of MKLP2-dependent Aurora B transport from chromatin to the anaphase central spindle. *J Cell Biol* **219**,.

Sha, Y.-W., Xu, X., Mei, L.-B., Li, P., Su, Z.-Y., He, X.-Q. and Li, L. (2017). A homozygous CEP135 mutation is associated with multiple morphological abnormalities of the sperm flagella (MMAF). *Gene* **633**, 48–53.

Sullivan, B. A. and Karpen, G. H. (2004). Centromeric chromatin exhibits a histone modification pattern that is distinct from both euchromatin and heterochromatin. *Nat Struct Mol Biol* **11**, 1076–83.

SY, L., CJ, Z., HY, P., H, S., KQ, L., XQ, H., K, H., JY, C. and ZQ, Y. (2017). Strong association of SLC1A1 and DPF3 gene variants with idiopathic male infertility in Han Chinese. *Asian J Androl* **19**, 486–492.

Trivedi, P. and Stukenberg, P. T. (2020). A Condensed View of the Chromosome Passenger Complex. *Trends Cell Biol* **30**, 676–687.

Vieira, A. R., McHenry, T. G., Daack-Hirsch, S., Murray, J. C. and Marazita, M. L. (2008). Candidate gene/loci studies in cleft lip/palate and dental anomalies finds novel susceptibility genes for clefts. *Genet Med* **10**, 668–74.

Vukušić, K., Buđa, R., Bosilj, A., Milas, A., Pavin, N. and Tolić, I. M. (2017). Microtubule Sliding within the Bridging Fiber Pushes Kinetochore Fibers Apart to Segregate Chromosomes. *Dev Cell* **43**, 11-23.e6.

Vukušić, K., Ponjavić, I., Buđa, R., Risteski, P. and Tolić, I. M. (2021). Microtubule-sliding modules based on kinesins EG5 and PRC1-dependent KIF4A drive human spindle elongation. *Dev Cell* **56**, 1253-1267.e10.

Warren, J. D., Orr, B. and Compton, D. A. (2020). A comparative analysis of methods to measure kinetochore-microtubule attachment stability. *Methods Cell Biol* **158**, 91–116.

Wei, R., Ngo, B., Wu, G. and Lee, W.-H. (2011). Phosphorylation of the Ndc80 complex protein, HEC1, by Nek2 kinase modulates chromosome alignment and signaling of the spindle assembly checkpoint. *Mol Biol Cell* **22**, 3584–94.

Woodruff, J. B., Ferreira Gomes, B., Widlund, P. O., Mahamid, J., Honigmann, A. and Hyman, A. A. (2017). The Centrosome Is a Selective Condensate that Nucleates Microtubules by Concentrating Tubulin. *Cell* **169**, 1066-1077.e10.

Yan, L., Xie, S., Du, Y. and Qian, C. (2017). Structural Insights into BAF47 and BAF155 Complex Formation. *J Mol Biol* **429**, 1650–1660.

Yang, Y., Roine, N. and Mäkelä, T. P. (2013). CCRK depletion inhibits glioblastoma cell proliferation in a cilium-dependent manner. *EMBO Rep* **14**, 741–747.

Yokoyama, H., Rybina, S., Santarella-Mellwig, R., Mattaj, I. W. and Karsenti, E. (2009). ISWI is a RanGTP-dependent MAP required for chromosome segregation. *J Cell Biol* **187**, 813–29.

Yokoyama, H., Nakos, K., Santarella-Mellwig, R., Rybina, S., Krijgsveld, J., Koffa, M. D. and Mattaj, I. W. (2013). CHD4 is a RanGTP-dependent MAP that stabilizes microtubules and regulates bipolar spindle formation. *Curr Biol* **23**, 2443–51.

Zeng, L., Zhang, Q., Li, S., Plotnikov, A. N., Walsh, M. J. and Zhou, M.-M. (2010). Mechanism and regulation of acetylated histone binding by the tandem PHD finger of DPF3b. *Nature* **466**, 258–62.

Zhao, H., Chen, Q., Li, F., Cui, L., Xie, L., Huang, Q., Liang, X., Zhou, J., Yan, X. and Zhu, X. (2021). Fibrogranular materials function as organizers to ensure the fidelity of multiciliary assembly. *Nat Commun* **12**, 1273.

Zhou, H., Zheng, T., Wang, T., Li, Q., Wang, F., Liang, X., Chen, J. and Teng, J. (2019a). CCDC74A/B are K-fiber crosslinkers required for chromosomal alignment. *BMC Biol* **17**, 1–14.

Zhou, H., Zheng, T., Wang, T., Li, Q., Wang, F., Liang, X., Chen, J. and Teng, J. (2019b). CCDC74A/B are K-fiber crosslinkers required for chromosomal alignment. *BMC Biol* **17**, 73.

Zhu, G., Conner, S. E., Zhou, X., Shih, C., Li, T., Anderson, B. D., Brooks, H. B., Campbell, R. M., Considine, E., Dempsey, J. A., et al. (2003). Synthesis, structure-activity relationship, and biological studies of indolocarbazoles as potent cyclin D1-CDK4 inhibitors. *J Med Chem* **46**, 2027–30.

Zhu, X., Lan, B., Yi, X., He, C., Dang, L., Zhou, X., Lu, Y., Sun, Y., Liu, Z., Bai, X., et al. (2020). HRP2-DPF3a-BAF complex coordinates histone modification and chromatin remodeling to regulate myogenic gene transcription. *Nucleic Acids Res* **48**, 6563–6582.

Figures

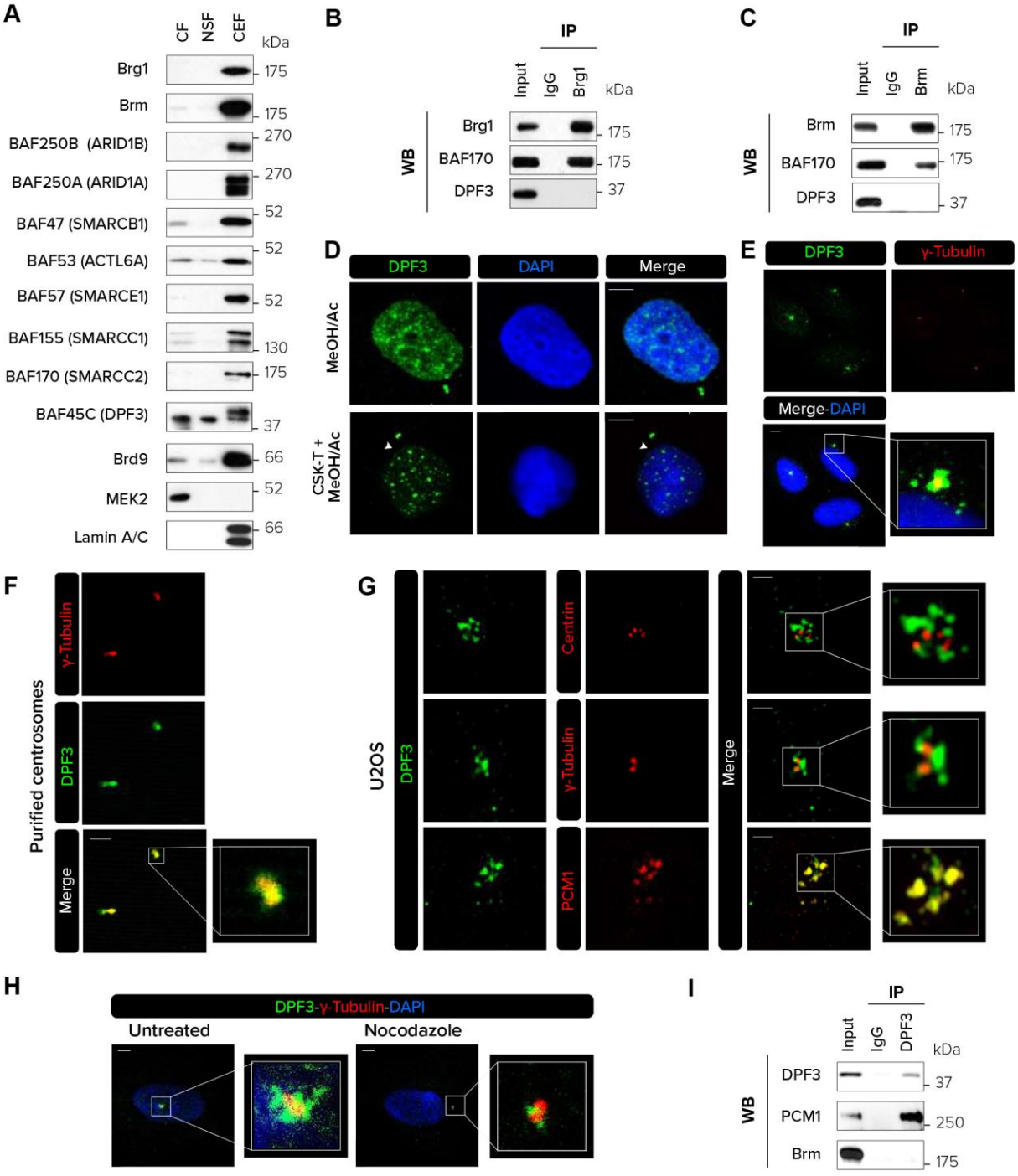

Fig. 1. DPF3 localizes to centriolar satellites in interphase

(**A**) Cytosolic fraction (CF), nuclear soluble fraction (NSF) and chromatin-enriched fractions (CEF) were isolated from U2OS cells and analyzed by western blotting for the indicated proteins. (**B-C**) Immunoprecipitation (IP) of endogenous Brm (**B**) or Brg1 (**C**) from U2OS cells followed by western blotting (WB) for Brm, Brg1, BAF170

or DPF3 proteins. (**D**) U2OS were pre-extracted or not with CSK buffer + Triton X100 (CSK-T), fixed with methanol/acetone (80/20) and stained for DPF3. Individual channels and merged channels are shown. White arrowheads indicate centrosomes. Scale bar = 5 µm. (**E-F**) Co-staining for DPF3 (in green) and γ-tubulin (in red) on U2OS cells (**E)** or isolated centrosomes purified from KE37 cells (**F)**. Individual channels, merged channels and magnification of boxed regions are shown. Scale bar = 2 µm. (**G**) U2OS cells were co-stained for DPF3 (in green) and centrin, γ-tubulin or PCM1 (in red). Individual channels, merged channels and magnification of boxed regions are shown. Scale bar = 2 µm. Image was captured with Zeiss LSM 880 Airyscan High Resolution (HR) microscope. **(H**) U2OS cells were treated with nocodazole (5 µg/mL) for 2 hours to depolymerize microtubule network. Cells were co-stained for DPF3 (in green) and γ-tubulin (in red). Merged channels with DAPI nuclear staining (in blue) and magnification of boxed regions are shown. Scale bar = 5 µm. (**I**) Immunoprecipitation (IP) of endogenous DPF3 from U2OS cells followed by western blotting (WB) for PCM1.

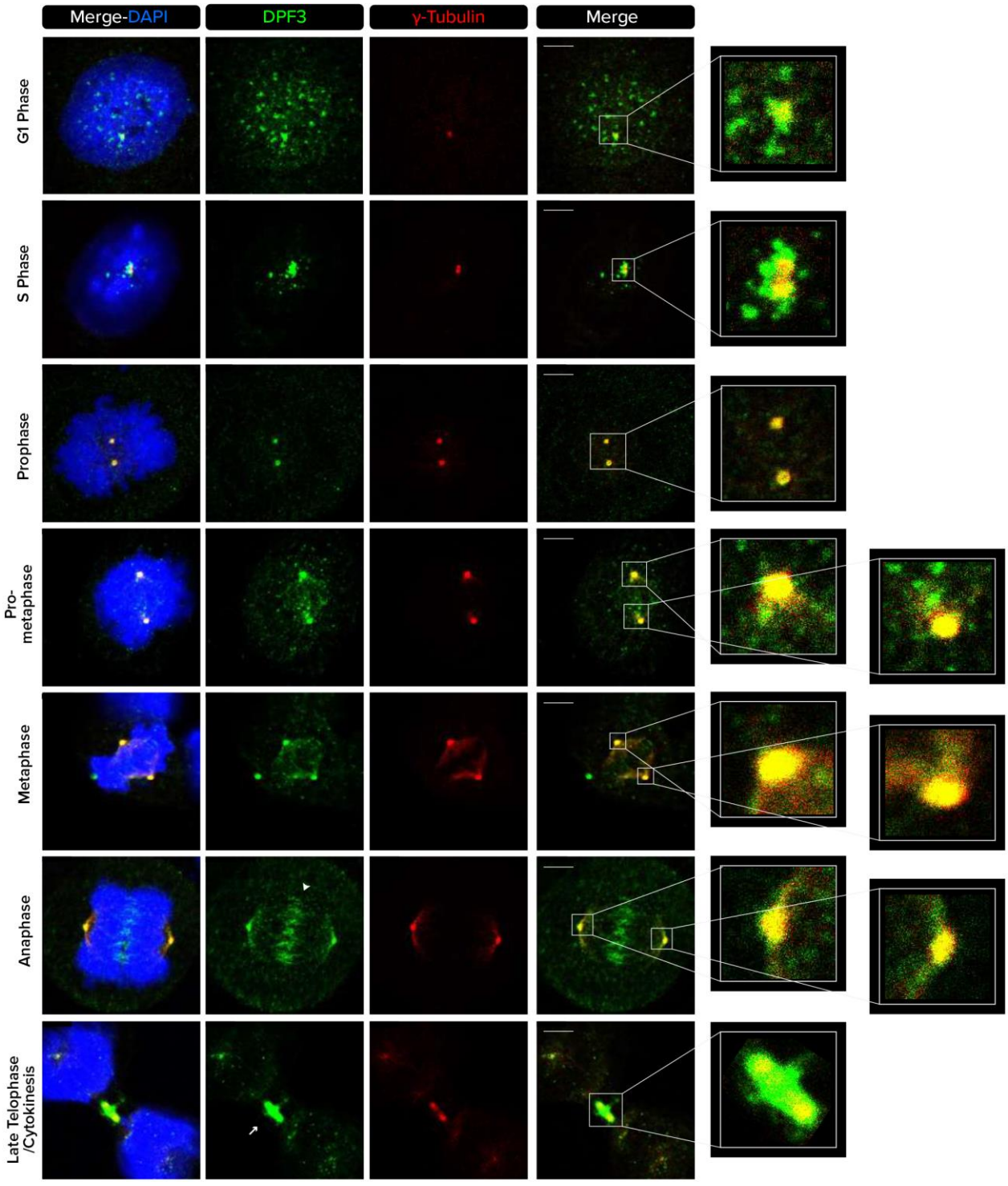

Fig. 2. DPF3 localizes to centrosomes and microtubule-based structures during mitotic cell division

U2OS cells were co-stained for DPF3 (in green) and γ-tubulin (in red). Individual channels, merged channels with DAPI nuclear staining (in blue), and magnification of boxed regions are shown. Scale bar = 5 µm. Nuclear condensation and position of γ-

tubulin identify cells in different cell cycle stages. White arrowhead indicates the position of the spindle midzone in anaphase. White arrow indicates the position of the midbody during cytokinesis.

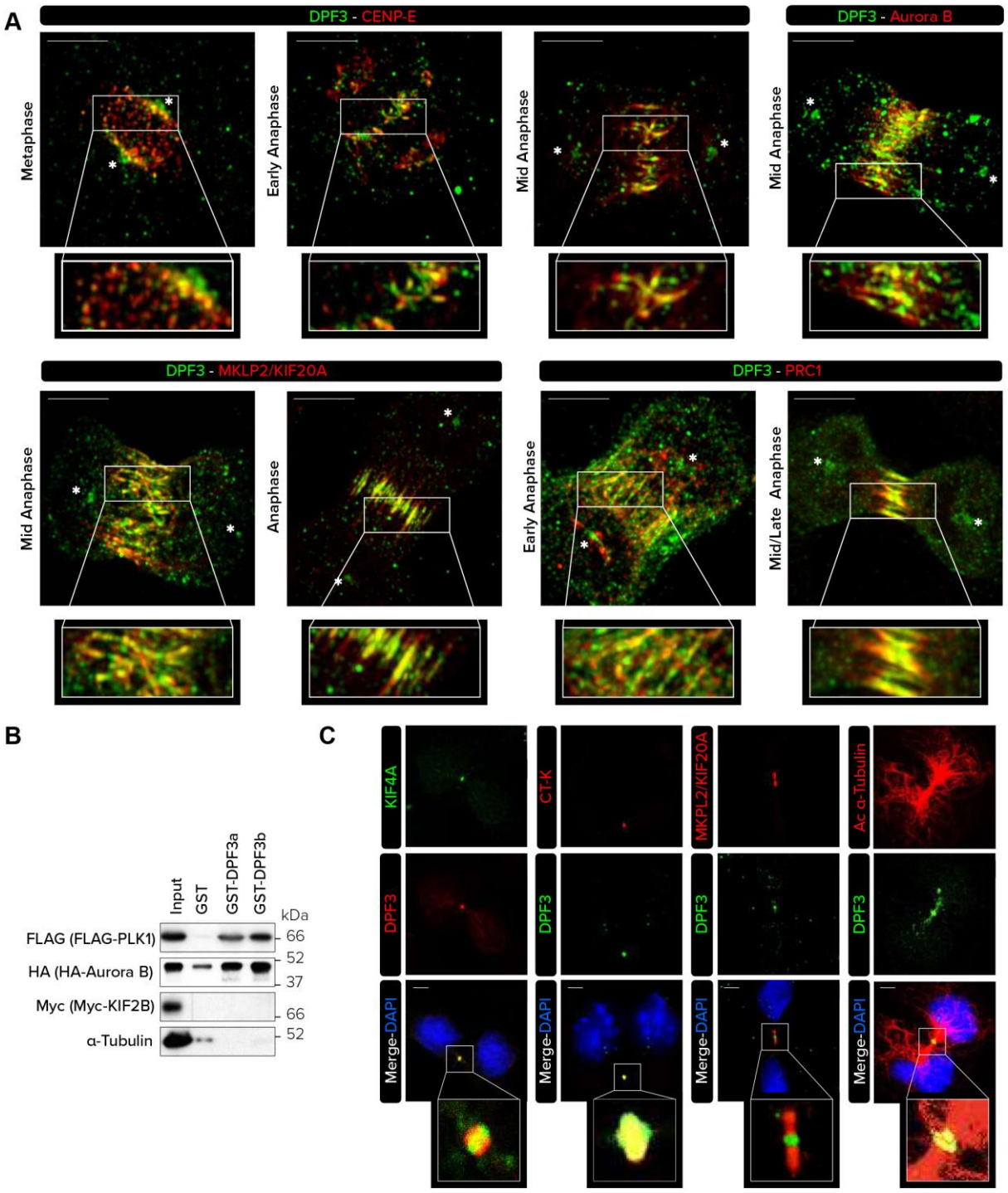

Fig. 3. DPF3 co-localizes with CPC complex and bridging fiber during metaphase

(**A**) HeLa cells were co-stained for DPF3 (in green) and CENP-E, Aurora B, MKPL2/KIF20A or PRC1 (in red). Merge channels and magnification of boxed regions are shown. Scale bar = 10 µm. Image was captured with Zeiss LSM 880 Airyscan High Resolution (HR) microscope. Stars (*) indicates centrosomes. (**B**)

Extracts from U2OS cells mock-transfected or transfected with FLAG-PLK1, HA-Aurora B or Myc-KIF2B plasmids were incubated with GSH beads conjugated with GST alone, GST-DPF3a or GST-DPF3b. Input and pulled-down proteins were detected by Western blotting using indicated antibodies. (**C**) U2OS cells were co-stained for DPF3 (in green or red) and KIF4A (in green), CT-K, MKPL2/KIF20A and acetylated α-tubulin (in red). Individual channels, merged channels with DAPI nuclear staining (in blue) and magnification of boxed regions are shown. Scale bar = 5 µm.

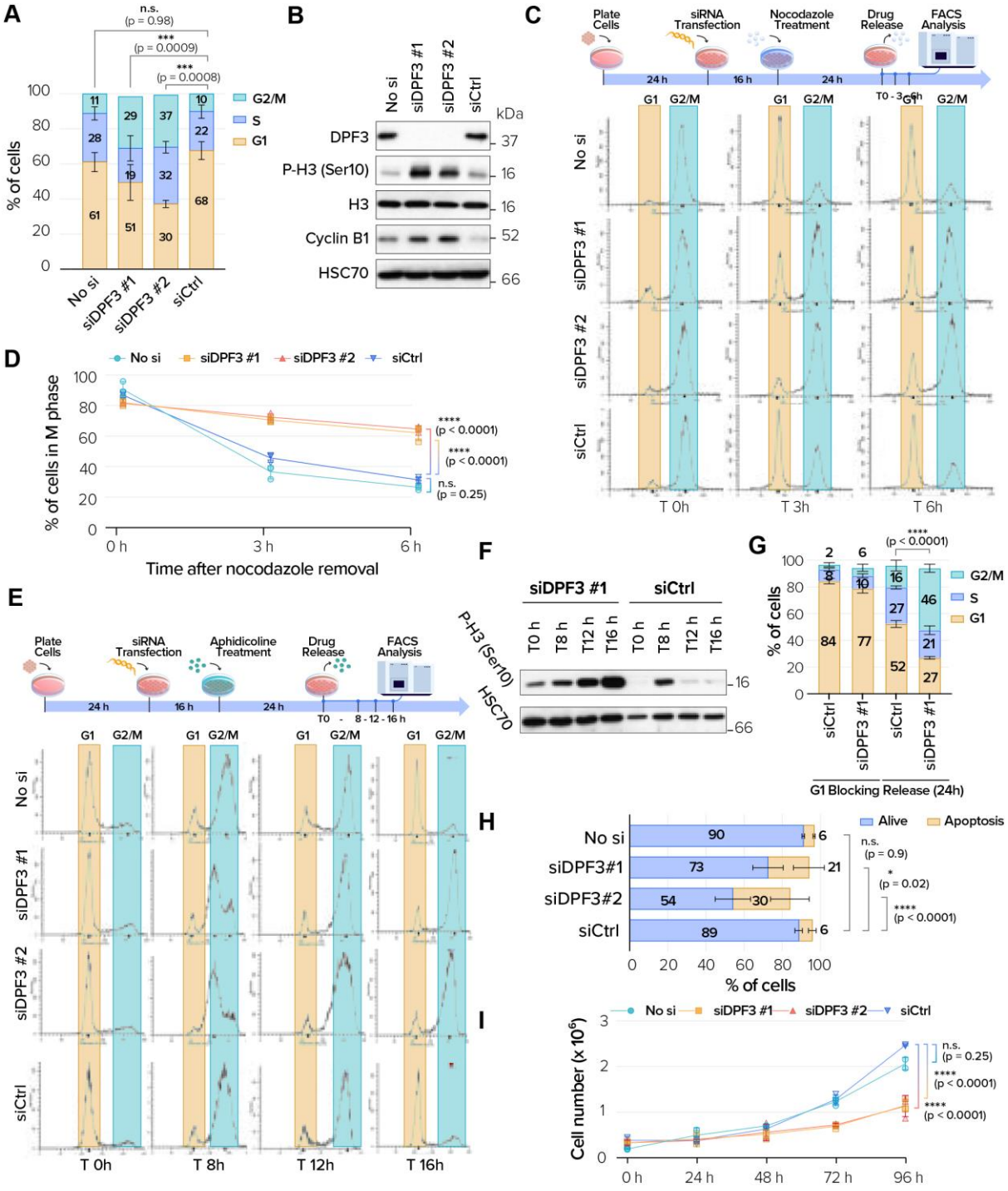

Fig. 4. DPF3 is required for faithful mitotic progression and genomic stability

(**A**) Cell cycle analysis of U2OS cells mock-transfected (No siRNA) or transfected with one of two different DPF3 siRNAs (siDPF3 #1 and siDPF3 #2) or control siRNA (siCtrl). Graph shows means +/- S.D. from 3 independent experiments. P-values were calculated using one-way ANOVA with Tukey post-hoc test. (**B**) Protein extracts from U2OS cells transfected as in A were analyzed by western blotting for the indicated proteins at the indicated time points. (**C**) U2OS cells were transfected as in

A. After transfection, cells were incubated for 24 hours with nocodazole (0.1 mg/mL). Cells were then released from the block by washing away the drug and changing to fresh complete medium. Samples were collected at the indicated times and processed for flow cytometry. FACS profiles are representative of one experiment performed in triplicates. (**D**) Quantification of FACS experiments as described in **C** shows the proportion of cells in G2/M at each of the indicated time points after nocodazole release. Graph shows means +/- S.D. from 3 independent experiments. P-values were calculated using one-way ANOVA with Tukey post-hoc test. (**E-F**) U2OS cells were transfected as in A. After transfection, cells were incubated for 24 hours with aphidicolin (1 ug/mL). Cells were then released from the block by washing away the drug and changing to fresh complete medium. Samples were collected at the indicated times and processed for flow cytometry. FACS profiles are representative of one experiment performed in triplicates **(E**). In parallel, protein extracts were prepared at the indicated times and analyzed by western blotting for the indicated proteins (**F**). (**G**) U2OS cells were transfected with control siRNA (siCtrl) or DPF3 siRNA (siDPF3 #1). After transfection, cells were incubated for 24 hours with CDK4 inhibitor CAS 546102-60-7 (5 μM). Cells were then released from the block by washing away the drug and changing to fresh complete medium. Samples were collected 24 hours later and processed for flow cytometry. Quantification of FACS experiments shows the proportion of cells in each cell cycle stage 24 hours after treatment with CDK4 inhibitor and 24 hours after the G1 release. Graph shows means +/- S.D. from 3 independent experiments. P-values were calculated using one-way ANOVA with Tukey post-hoc test. (**H**) Quantification of apoptotic cell death in U2OS cells transfected as in A. Graph shows means +/- S.D. from 3 independent experiments. P-values were calculated using two-way ANOVA with Dunnett's post-hoc test. (**I**) Growth curve analysis of HeLa cells transfected as in A. Graph shows means +/- S.D. from 3 independent experiments. P-values were calculated using one-way ANOVA with Tukey post-hoc test.

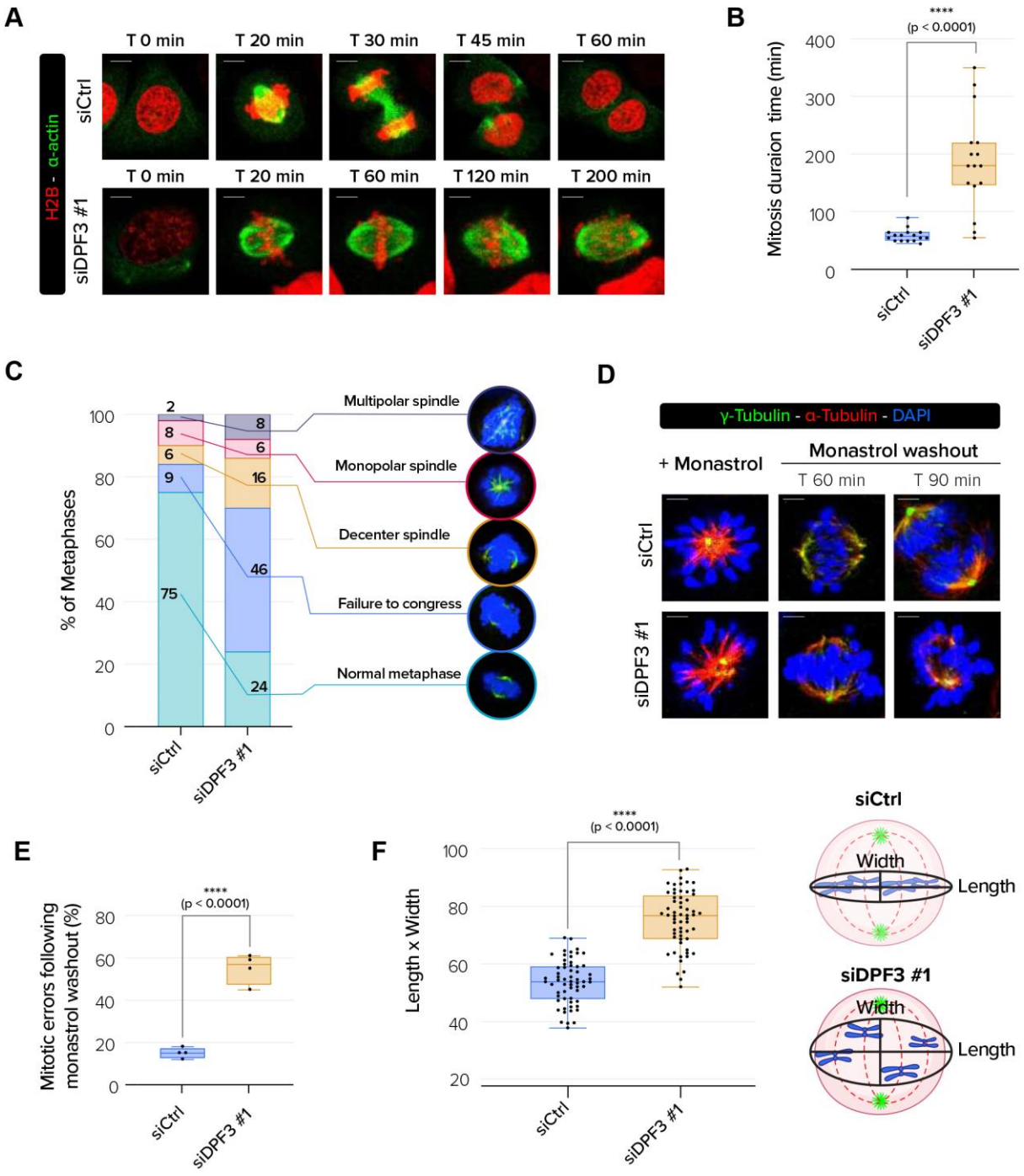

Fig. 5. DPF3 is required for chromosome alignment

(**A**) Live imaging experiments of H2B-RFP/α-actin-GFP U2OS cells transfected with control siRNA (siCtrl) or DPF3 siRNA (siDPF3 #1) beginning 48 hours post-transfection. Scale bar = 5 µm. (**B**) Mitotic duration for H2AB-RFP/α-actin-GFP U2OS cells transfected as in A (n = 16 cells/ condition). P-values were calculated using unpaired two-tailed t-test. Box limits = 25th to 75th percentiles; line = median; whiskers = min to max. (**C**) Quantification of the percentage of aberrant mitotic

phenotype in U2OS cells transfected as in A (n = 100 cells/conditions for one experiment). Representative images of abnormal mitotic phenotypes that were quantified are shown. (**D**) U2OS cells transfected with control siRNA (siCtrl) or DPF3 siRNA (siDPF3 #1) and treated with monastrol (100 μM) for 3 hours and then released in fresh culture medium. Cells were co-stained prior to monastrol washout and at 60 min or 90 min after washout. Mitotic spindles were labeled with α-tubulin (in red), centrosome with γ-tubulin (in green), and chromosomes with DAPI (in blue). Merged channels with DAPI nuclear staining (in blue) are shown. Scale bar = 5 μm. (**E**) Quantification of the mitotic errors on monastrol washout from the experiment described in D. Graph shows means +/- S.D from 3 independent experiments (n = total of 70 cells for each condition). P-value calculated using unpaired two-tailed t-test. Box limits = 25th to 75th percentiles; line = median; whiskers = min to max. (**F**) Quantification of chromosome mis-alignment. A ratio was determined as schematized in the right panel and calculated in each condition. Graph shows means +/- S.D from 3 independent experiments (n = 20 cells/condition/experiments). P-value calculated using unpaired two-tailed t-test. Box limits = 25th to 75th percentiles; line = median; whiskers = min to max.

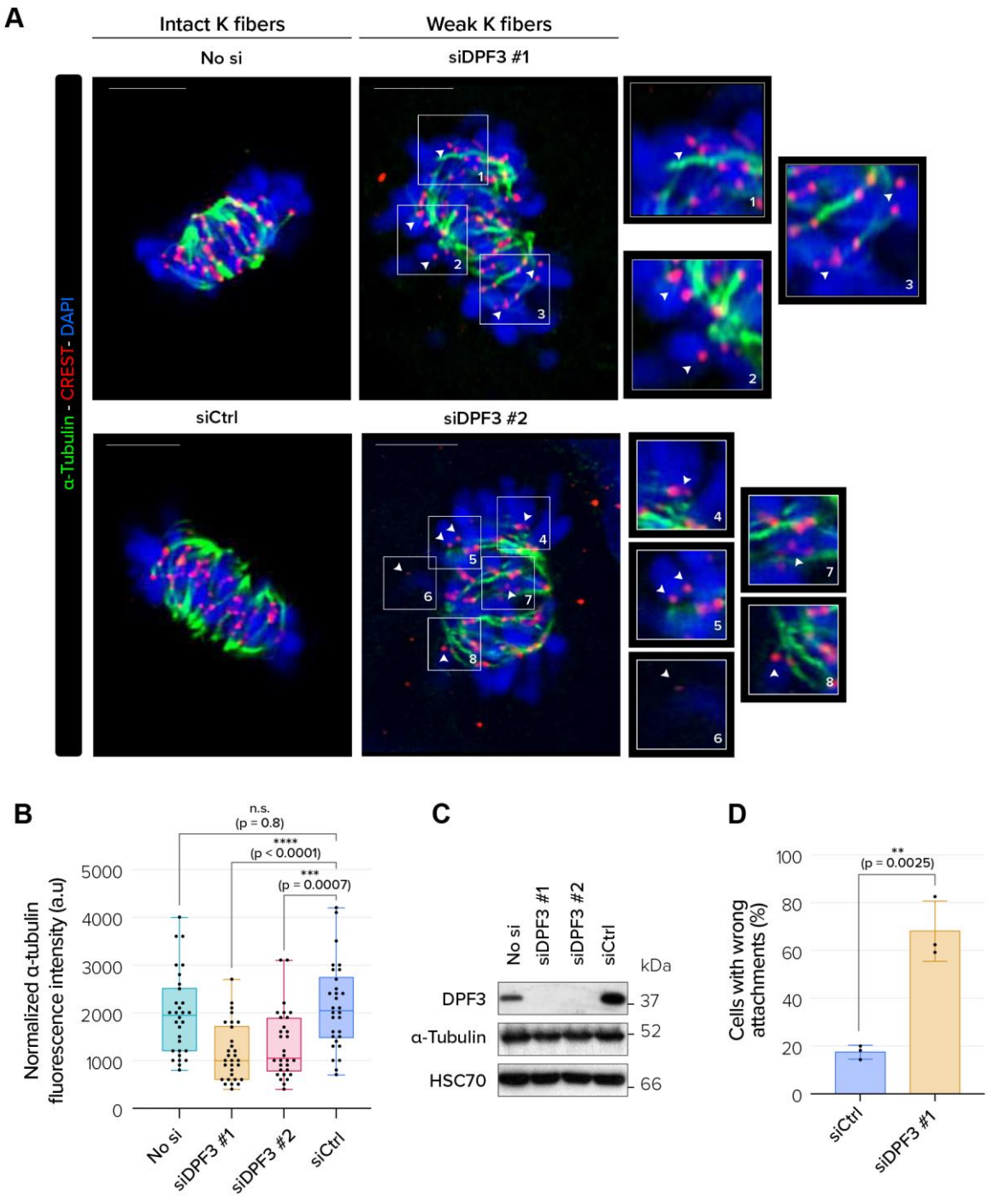

Fig. 6. DPF3 is required for stabilizing K-fibers and robust KT–MT attachments in metaphase

(**A**) U2OS cells were mock-transfected (No si) or transfected with one of two different DPF3 siRNAs (siDPF3 #1 and siDPF3 #2) or control siRNA (siCtrl) and then subjected to cold stable microtubule assay after mitotic arrest in metaphase. Mitotic spindles were labeled with α-tubulin (in green), kinetochores with CREST (in red), and chromosomes with DAPI (in blue). Merged images of maximum intensity

projections of Z-stack planes (0.25 µm interval) are shown. Scale bar = 5 µm. White arrowheads and magnification of boxed areas showed less stable and robust KT–MT attachment. (**B**) Quantification of α-tubulin fluorescence intensity in U2OS cells mock-transfected (No si) or transfected with one of two different DPF3 siRNAs (siDPF3 #1 and siDPF3 #2) or control siRNA (siCtrl). Graph shows means +/- S.D. from 3 independent experiments (n = 10 cells/ condition/experiments). P-values were calculated using one-way ANOVA with Tukey post-hoc test. Box limits = 25th to 75th percentiles; line = median; whiskers = min to max. (**C**) Protein extracts from U2OS cells mock-transfected (No siRNA) or transfected with one of two different DPF3 siRNAs (siDPF3 #1 and siDPF3 #2) or control siRNA (siCtrl) were analyzed by western blotting for the indicated proteins. (**D**) Quantification of the rate of defective KT–MT attachment in U2OS cells transfected as in A. Graph shows means +/- S.D. from 3 independent experiments (n = > 20 cells/ condition/experiments). P-values were calculated using unpaired two-tailed t-test.

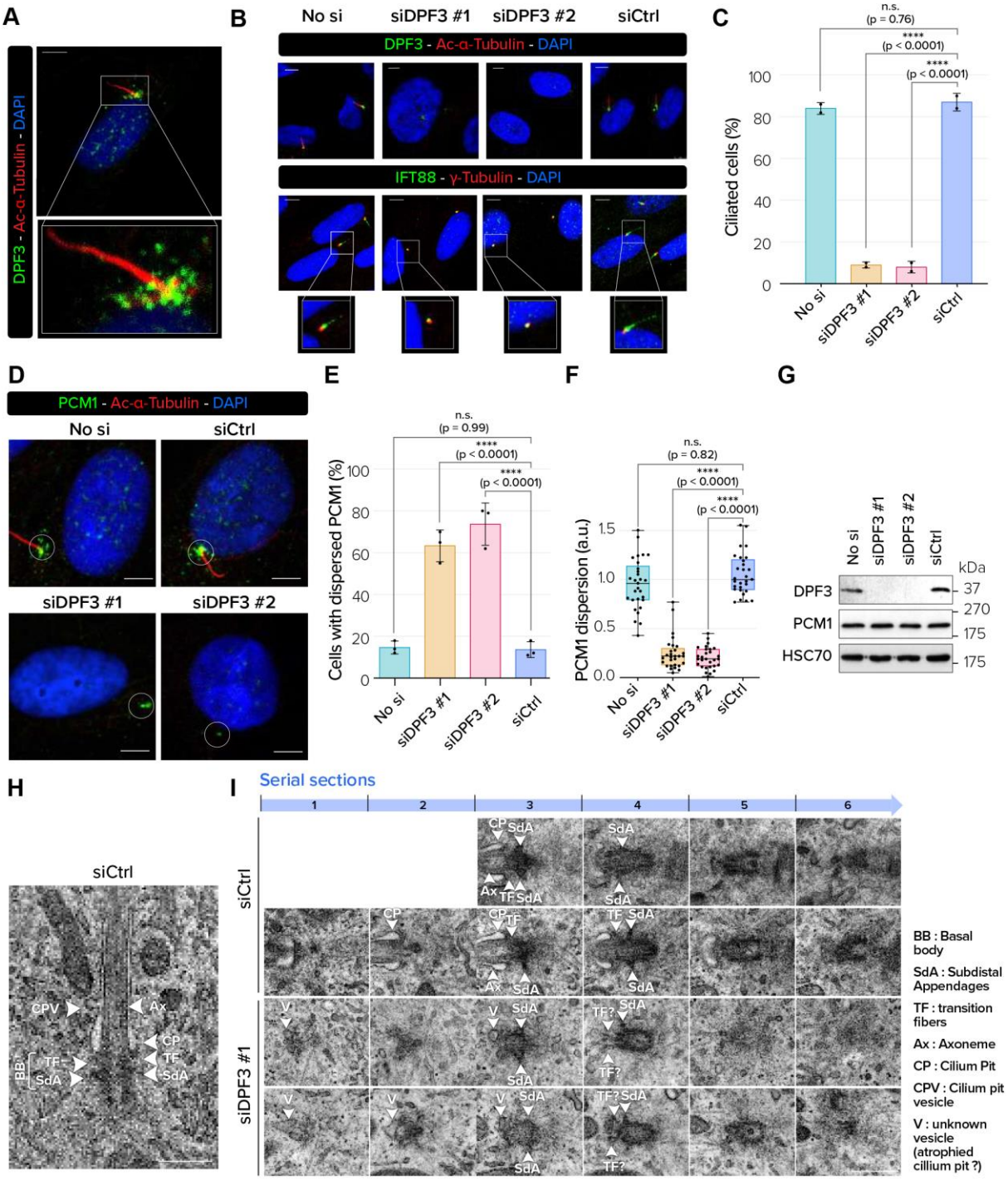

Fig. 7. DPF3 depletion disrupts centriolar satellite stability and primary cilia formation by blocking axoneme extension

(**A**) Serum-starved ciliated hTERT-RPE-1 cells were co-stained for DPF3 (in green) and acetylated α-tubulin (in red). Merged channels with DAPI nuclear staining (in blue) and magnification of boxed regions are shown. Scale bar = 5 µm. (**B**) hTERT-RPE-1 cells were mock-transfected (No si) or transfected with one of two different DPF3 siRNAs (siDPF3 #1 and siDPF3 #2) or control siRNA (siCtrl), serum starved

for 48 hours and co-stained for DPF3 (in green) and acetylated α-tubulin (in red) or IFT88 (in green) and γ-tubulin (in red). Merged channels with DAPI nuclear staining (in blue) are shown. Scale bar = 5 µm. (**C**) Quantification of the percentage of ciliated hTERT-RPE-1 cells after siRNAs transfection as described in B. Graph shows means +/- S.D. from 3 independent experiments (n = 50 cells/condition/experiments). P-values were calculated using one-way ANOVA with Tukey post-hoc test. **(D**) hTERT-RPE-1 cells were treated as in B and co-stained for PCM1 (in green) and acetylated α-tubulin (in red). Merged channels with DAPI nuclear staining (in blue) are shown. White arrowheads indicate widely dispersed PCM1 granules. Scale bar = 5 µm. (**E**) Quantification of hTERT-RPE-1 cells with dispersed PCM1 profiles after siRNAs transfection. Graph shows means +/- S.D. from 3 independent experiments (n = 100 cells/condition/experiments). P-values were calculated using one-way ANOVA with Tukey post-hoc test. (**F**) The pericentrosomal fluorescence intensity of PCM1 was measured in circle area drawn around the centrosome, and signal level was normalized to 1 in 'No si' condition. Graph shows means +/- S.D. from 3 independent experiments (n = 10 cells/condition/experiments). P-values were calculated using one-way ANOVA with Tukey post-hoc test. Box limits = 25th to 75th percentiles; line = median; whiskers = min to max. (**G**) Protein extracts from hTERT-RPE-1 cells transfected as described in B. were analyzed by western blotting for the indicated proteins. (**H**-**I**) Transmission electron micrographs of mother centrioles and axoneme (serial sections) in hTERT-RPE-1 cells transfected with control siRNA (siCtrl) or DPF3 siRNA (siDPF3 #1). White arrowheads indicate different ciliary structures described in the panel legend. Scale bar = 500 nm.

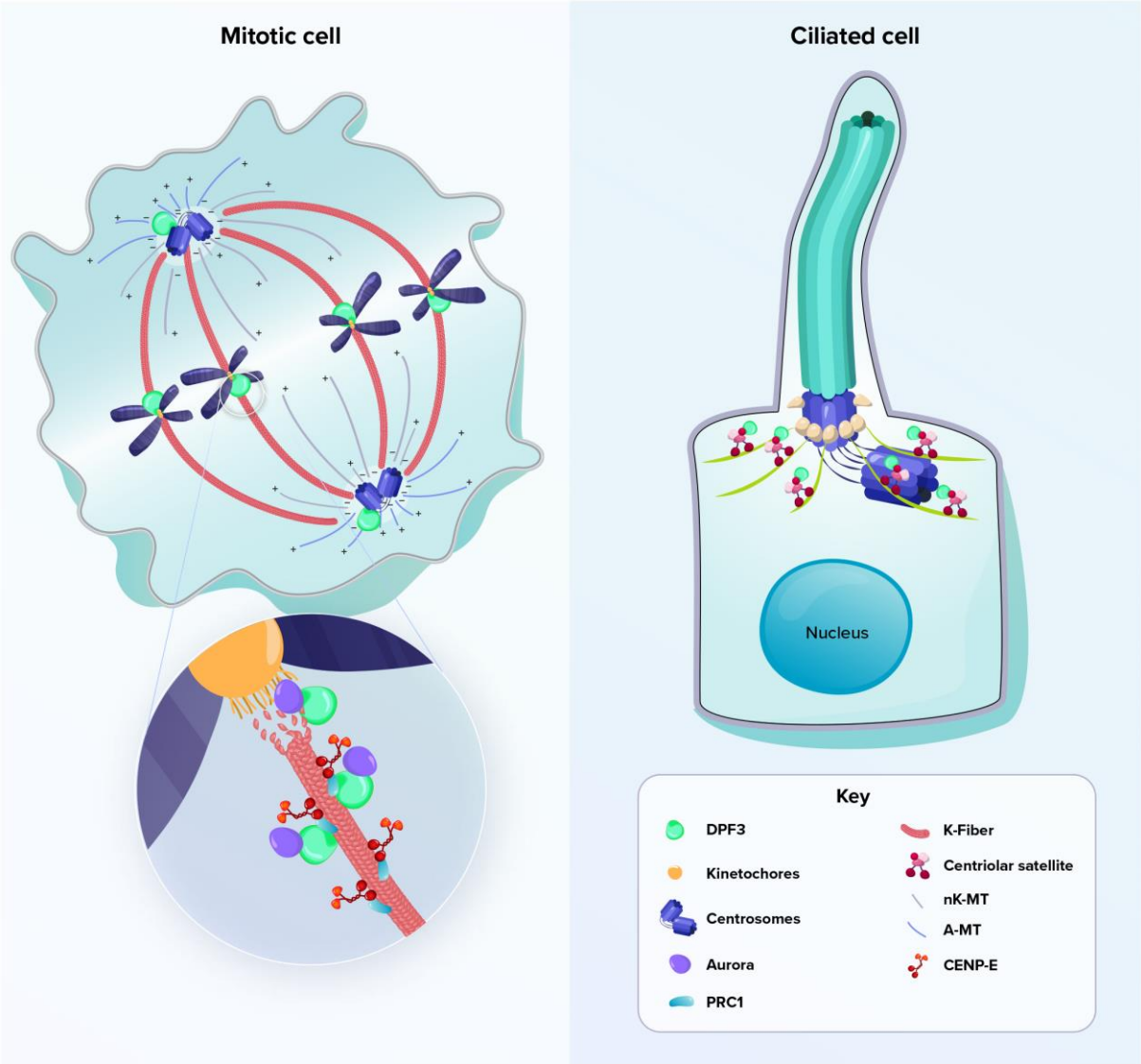

Fig. 8. Schematic representation of DPF3 localization during mitosis and ciliogenesis. (**A**) DPF3 is located in centrosome and spindle midzone in mitotic cells. During metaphase to anaphase transition, DPF3 is present at a microtubule-binding interface and might connect the CPC molecular complex to the chromosomes/kinetochores structure. (**B**) In ciliated cells, DPF3 is located in centriolar satellites.

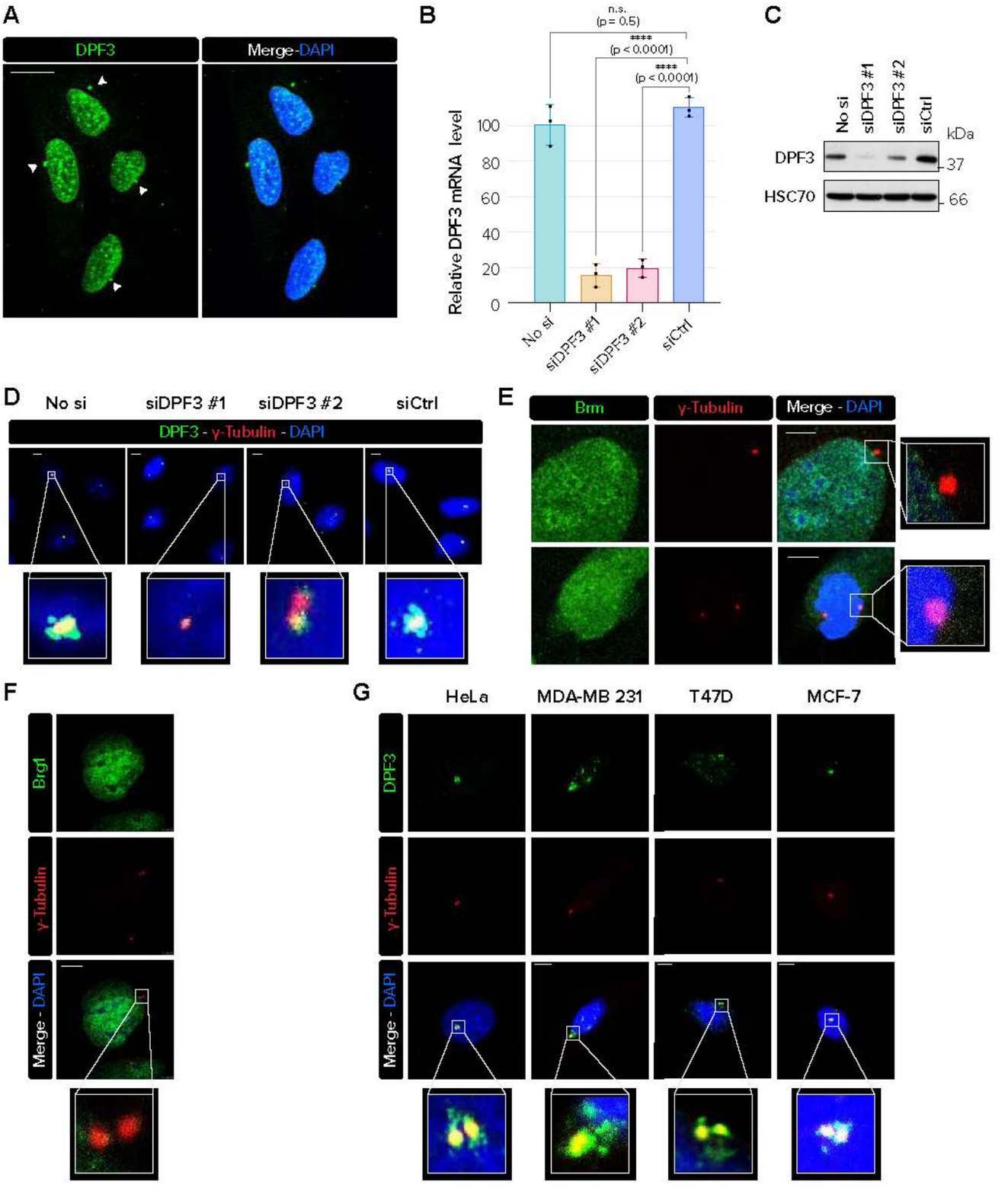

Fig. S1. Localization of DPF3 and other BAF subunits and specificity of the DPF3 staining at centrosome

(A) U2OS were fixed with methanol/acetone (80/20) and stained for DPF3. Several cells are shown and are representative of the total population. Individual channels for DPF3 (in green) and merged channels with DAPI nuclear staining (in blue) are shown. Scale bar = 10 µm. (**B-C**) U2OS

cells were mock-transfected (No si) or transfected with one of two different DPF3 siRNAs (siDPF3 #1 and siDPF3 #2) or control siRNA (siCtrl). RNA and protein extracts were prepared in parallel and analyzed by RT-qPCR (**B**) or western blotting (**C**), respectively. (**D**) U2OS cells were mock-transfected (No si) or transfected with one of two different DPF3 siRNAs (siDPF3 #1 and siDPF3 #2) or control siRNA (siCtrl) and co-stained for DPF3 (in green) and γ-tubulin (in red). Merged channels with DAPI nuclear staining (in blue) and magnification of boxed regions are shown. Scale bar = 5 µm. (**E**) U2OS cells co-stained for Brm (in green) and γ-tubulin (in red). Individual channels, merged channels with DAPI nuclear staining (in blue) and magnification of boxed regions are shown. Scale bar = 10 µm. (**F**) U2OS cells co-stained for Brg1 (in green) and γ-tubulin (in red). Individual channels, merged channels with DAPI nuclear staining (in blue) and magnification of boxed regions are shown. Scale bar = 5 µm. (**G**) DPF3 (in green) and γ-tubulin (in red) were co-stained in HeLa, MDA-MB 231, T47D and MCF-7 (from top to bottom). Individual channels, merged channels with DAPI nuclear staining (in blue) and magnification of boxed regions are shown. Scale bar = 5 µm.

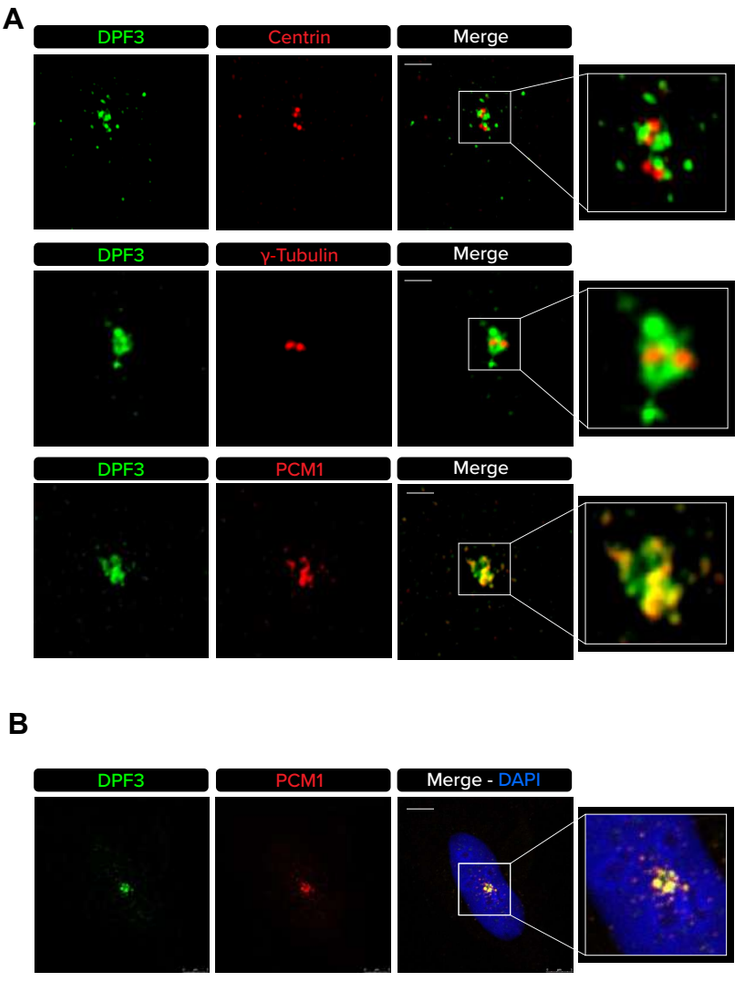

Fig. S2. Co-localization of DPF3 with centriolar satellites in HeLa cells

(**A**) HeLa cells co-stained for DPF3 (in green) and centrin, γ-tubulin or PCM1 (in red). Individual channels, merged channels and magnification of boxed regions are shown. Scale bar = 2 µm. Image was captured with Zeiss LSM 880 Airyscan High Resolution (HR) microscope. (**B**) HeLa cells were co-stained for DPF3 (in green) and PCM1 (in red). Individual channels, merged channels with DAPI nuclear staining (in blue), and magnification of boxed regions are shown. Scale bar = 5 µm. Image was captured with Leica TCS SP5 laser scanning confocal microscope.

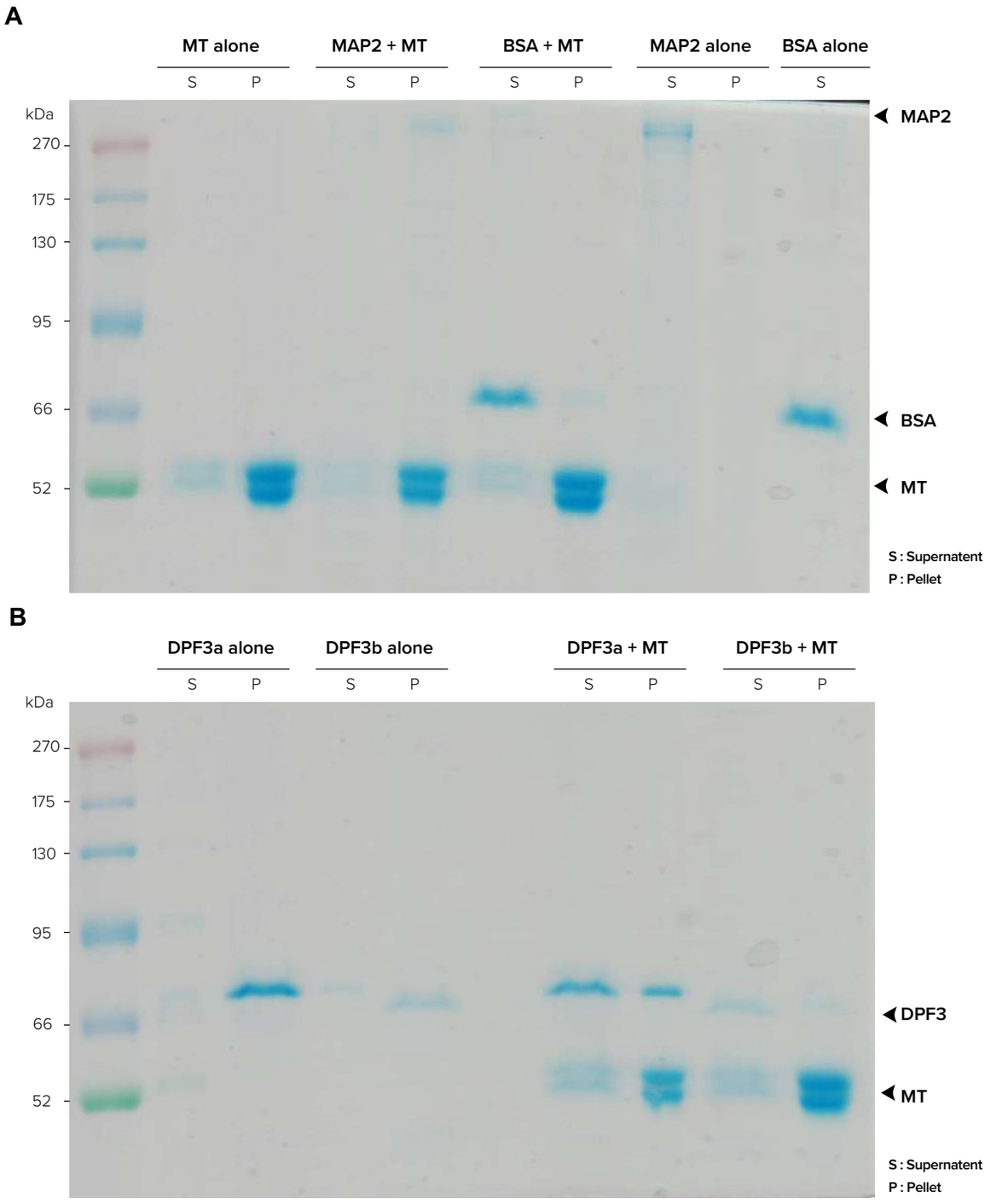

Fig. S3. DPF3a and to a lesser extend DPF3b interact with microtubules

(**A**) Taxol-stabilized microtubules were incubated or not with purified MAP2 (positive control) or BSA (negative control) and sedimented by ultracentrifugation. The supernatant (S) and pellet (P) fractions were run on a SDS gel and stained with Coomassie blue. **(B)** Taxol-stabilized microtubules were incubated or not with purified GST-DPF3a or GST-DPF3b and sedimented by ultracentrifugation. The supernatant (S) and pellet (P) fractions were analyzed by SDS-PAGE followed by Coomassie blue staining.

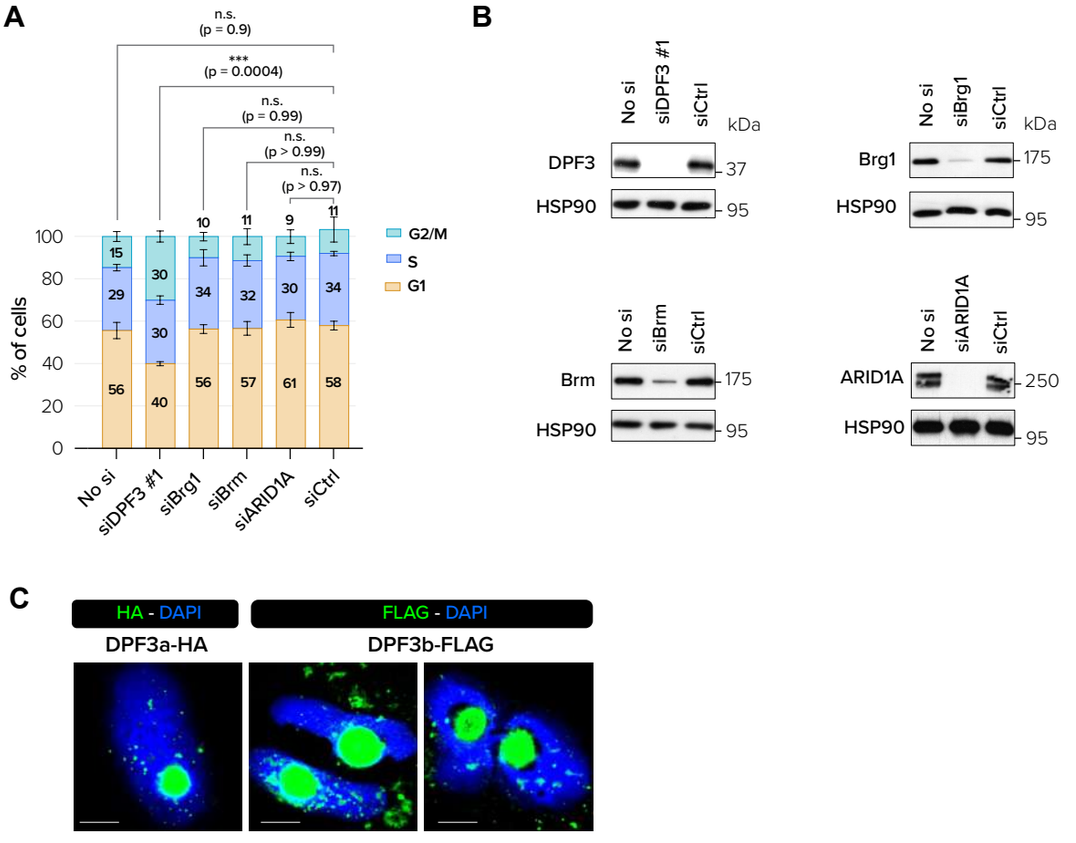

Fig. S4. Depletion of DPF3 but not the core subunits of the BAF complex blocks cells in G2/M (**A**) Cell cycle analysis of U2OS cells transfected with control siRNA (siCtrl), DPF3 siRNA (siDPF3 #1), Brm siRNA, Brg1 siRNA, or ARID1A siRNA. Graph shows means +/- S.D. from 3 independent experiments. P-values were calculated using one-way ANOVA with Tukey post-hoc test. (**B**) In parallel, protein from U2OS cells transfected as in A were extracted and analyzed by western blotting for the indicated proteins. (**C**) U2OS cells were transfected with DPF3-HA or DPF3B-FLAG plasmids for 24 hours and processed for immunofluorescence staining using HA or FLAG antibodies (in green). Merged channels with DAPI nuclear staining (in blue) are shown. Scale bar = 5 µm

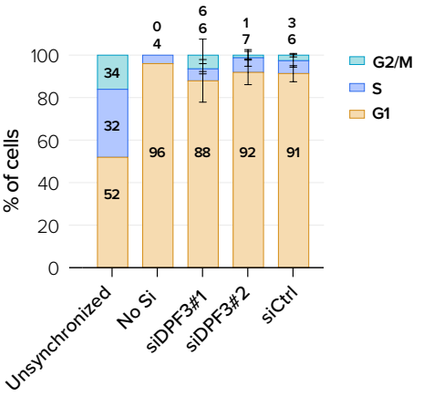

Fig. S5. Serum starvation blocks DPF3-depleted hTEÒRT-RPE-1 cells in G0/G1

Cell cycle analysis of asynchronous hTERT-RPE-1 cells or hTERT-RPE-1 cells mock-transfected (No si) or transfected with one of two different DPF3 siRNAs (siDPF3 #1 and siDPF3 #2) or control siRNA (siCtrl) and serum starved for 48 hours. Results are representative of one experiment performed twice.

Table S1. siRNA sequences

siRNA	Sense Sequence 5' → 3'	Anti-sense Sequence 3' → 5'
ARID1A	GCCCUGAACAAUAACCUCA	UGAGGUUAUUGUUCAGGGC
Brm	GUCCUGGACCUCCAAGUGUCU	AGACACUUGGAGGUCCAGGAC
Brg1	Santa Cruz Biotechnology (#sc-29827)	
DPF3 #1	CCCAGAACAACUGCUACAUTT	AUGUAGCAGUUGUUCUGGGTT
DPF3 #2	GGAGGAAAGCAUCCAGGAATT	UUCCUGGAUGCUUUCCUCCTT
Gl3 (siCtrl)	CUUACGCUGAGUACUUCGAU	AAUCGAAGUACUCAGCGUAAU

Table S2. Sequences of primers used in qPCR experiments

mRNA	Reverse sequence 5' → 3'	Forward Sequence 5' → 3'
DPF3a/b	TTCCTGGATGCTTTCCTCCT	GGCTGCTGGAGATAAAACCTGA
β-actin	AGAGGCGTACAGGGATAGCA	AGAAAATCTGGCACCACACC

Table S3. Antibodies used in western blotting experiments

Antibody	Company	Catalogue number	RRID	Working dilution
α-tubulin (11H10)	Cell Signaling	#2125	AB_2619646	1:5000
β-actin	Santa Cruz	#sc-69879	AB_2714189	1:5000
ARID1A	Abcam	#Ab182560		1:1000
ARID1B	Novus a bio-techne brand	#NBP1-89358	AB_11032492	1:1000
BAF47	Cell Signaling	#91735	AB_2800172	1:1000
BAF53	Cell Signaling	#43910	AB_2799251	1:1000
BAF57	Bethyl	#A300-810A-T	AB_2779472	1:1000
BAF155	Cell Signaling	#11956	AB_2797776	1:1000
BAF170	Cell Signaling	#12760	AB_2798017	1:1000
Brd9	Cell Signaling	#71232	AB_2799798	1:1000
Brg1	Cell Signaling	#3508	AB_2193944	1:1000

Journal of Cell Science • Supplementary information

Brg1 (E8V5B)	Cell Signaling	#72182	AB_2799815	1:1000
Brm	Novus a bio-techne brand	#NBP1-90015	AB_11031434	1:1000
Brm	BD transduction laboratories	#610389	AB_397772	1:2000
Cylin B1	Santa Cruz Biotechnology	#sc-752	AB_2072134	1:1000
DPF3 (E7F7N)	Cell Signaling	#82788		1:500
FLAG	Sigma	#F1804	AB_262044	1:2000
HA (C29F4)	Cell Signaling	#3724	AB_1549585	1:1000
Histone H3	Cell Signaling	#9715	AB_331563	1:2000
Phospho-H3 (Ser10)	Cell Signaling	#3377	AB_1549592	1:2000
HSC70	Santa Cruz	#sc-7298	AB_627761	1:5000
Lamin A/C	Millipore	#MAB3211	AB_94752	1:1000
Mek2	Santa Cruz	#sc-13159	AB_627923	1:1000
c-Myc(Y69)	Abcam	#ab32072	AB_731658	1:1000
PCM1	Cell Signaling	#5213	AB_10556960	1:1000
Secondary antibodies conjugated with horseradish peroxidase (HRP)	Anti-*Rabbit HRP* Antibody Anti-Mouse HRP Antibody Rabbit anti-goat IgG HRP-linked	Cell Signaling *#7074* Dako #P0260 Life Technologies #31402	AB_2099233 AB_2636929 AB_228395	All used 1:5000 to 1:10,000

Table S4. Antibodies used in immunoprecipitation experiments

Antibody	Company	Catalogue number	RRID	Working dilution
Brm (D9E8B)	Cell Signaling	#11966	AB_2797783	2-4 μg/ IP
Brg1 (D1Q7F)	Cell Signaling	#49360	AB_2728743	2-4 μg/ IP
DPF3 (E7F7N)	Cell Signaling	#82788		2 μg/ IP

Table S5. Antibodies used in immunofluorescence experiments

Antibody	Company	Catalogue number	RRID	Working dilution
α-tubulin (11H10)	Cell Signaling	#2125	AB_2619646	1:500
α-tubulin (DM1A)	Cell Signaling	#3873	AB_1904178	1:500
Y-tubulin	Santa Cruz	#sc-51715	AB_630410	1:500
Y-tubulin	Genetex	#GTX113286	AB_1952442	1:500
Acetylated α-tubulin	Santa Cruz	#sc-23950	AB_628409	1:500
Aurora B	Abcam	#ab3609	AB_449204	1:100
CENP-A	Invitrogen	#MA1-20832	AB_2078763	1:500
CENP-E	Active Motif	# 39619	AB_2793278	1:200
Centrin-2	Millipore	#04-1624	AB_10563501	1:100
CREST	Immunovision	#HCT-0100	*AB_2744669*	1:1000
CT-K	BD transduction laboratories	#61376		1:500
DPF3	Biorbyt	#Orb182556		1:200
FLAG	Sigma	#F1804	AB_262044	1:500
HA	Cell Signaling	#3724	AB_1549585	1:500
IFT88	Proteintech	#13967-1-AP	AB_2121979	1:500
KIF4A	Novus a bio-techne brand	#NBP2-56589		1:500
MKPL2/KIF20A	Abnova	#H00010112-B01	AB_1146023	1:500
PCM1	Santa Cruz Biotechnology	#sc-398365	AB_2827155	1:500
PRC1	Invitrogen	# **MA1-846**	AB_1086772	1:200
Secondary antibodies	Thermo Fisher Scientific	Goat anti Rabbit IgG Alexa Fluor 488 conjugate #A-	AB_2576217	

conjugated with Alexa dyes		11034 Donkey anti-rabbit IgG, Alexa Fluor 488 conjugate #A-21206 Goat anti-Mouse IgG, Alexa Fluor 488 conjugate #A-11001 Donkey anti-Mouse IgG, Alexa Fluor 546 conjugate #A-10036 Goat anti-rabbit IgG, Alexa Fluor 546 conjugate #A-11035	AB_2535792 AB_2534069 AB_2534012 AB_143051	All used 1:2000

Blots in Fig. 1

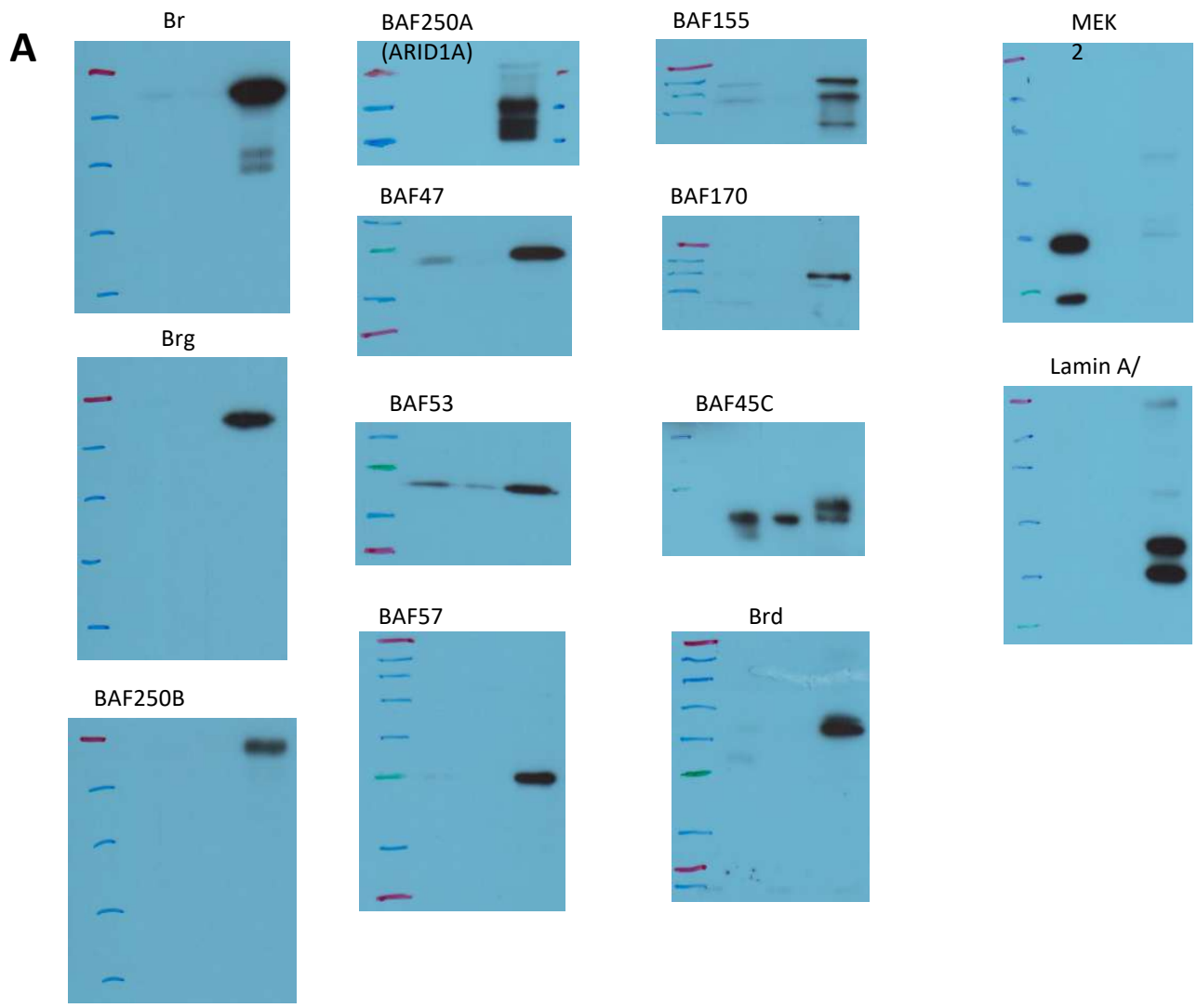

Blots in Fig. 1

B

BRG1 (IP BRG1)

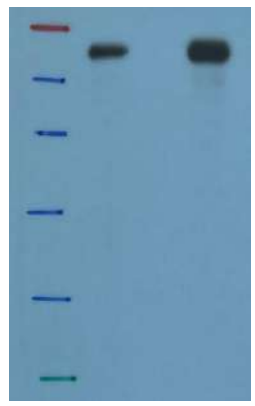

BAF170 (IP BRG1)

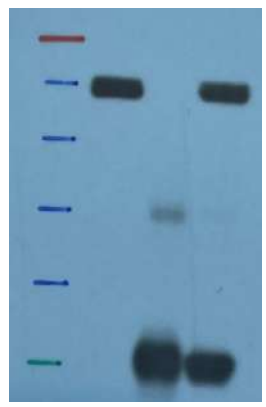

DPF3 (IP BRG1)

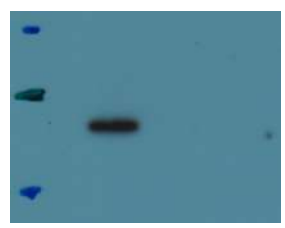

C

BRM (IP BRM)

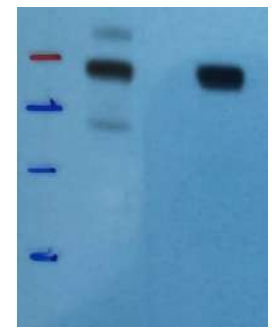

BAF 170 (IP BRM)

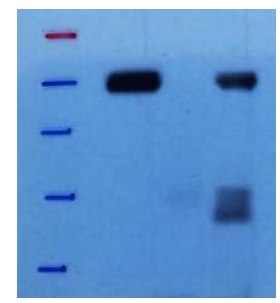

H

BRM(IP DPF3)

PCM1(IP DPF3)

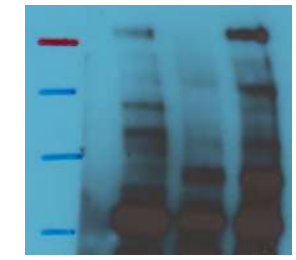

DPF3 (IP DPF3)

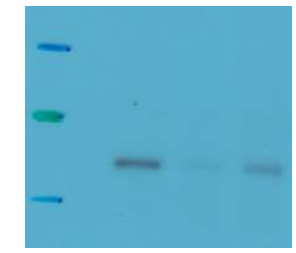

Blots in Fig. 3

B

PLK1 (FLAG)

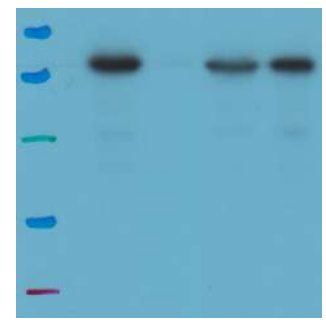

Aurora A (HA)

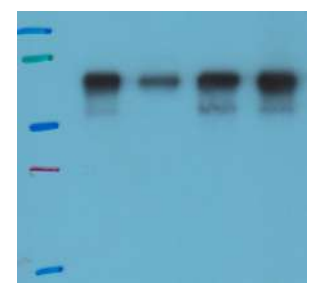

KIF2B (Myc)

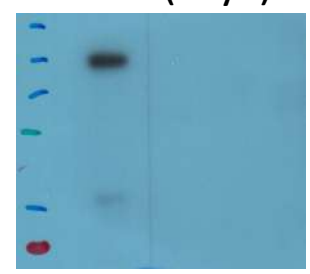

α-Tubulin

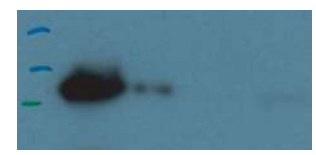

Journal of Cell Science • Supplementary information

Blots in Fig. 4

B

DPF3

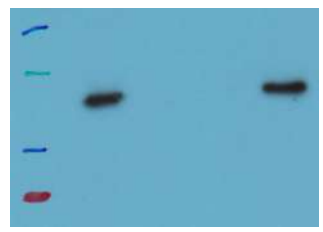

P-Histone H3 Ser 10

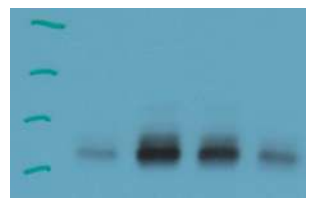

Histone H3

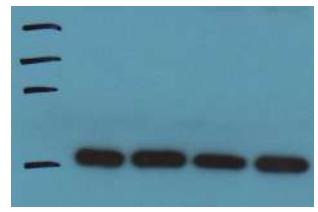

Cyclin B1

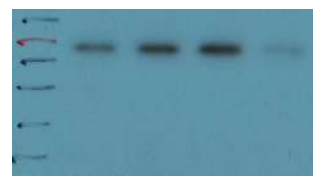

HSC70

F

P-Histone H3 Ser 10

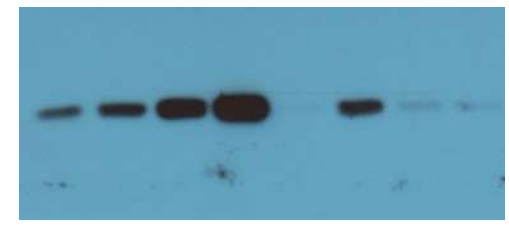

HSC70

Blots in Fig. 6

C

DPF3

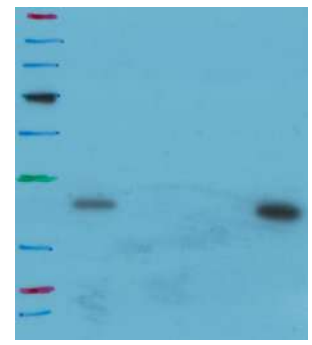

Alpha-Tubulin

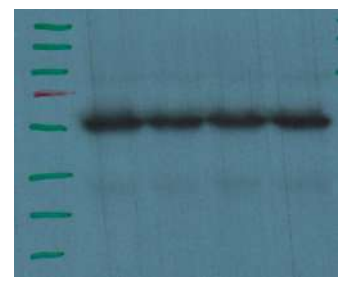

HSC70

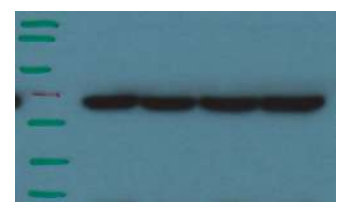

Blots in Fig. 7

G

DPF3

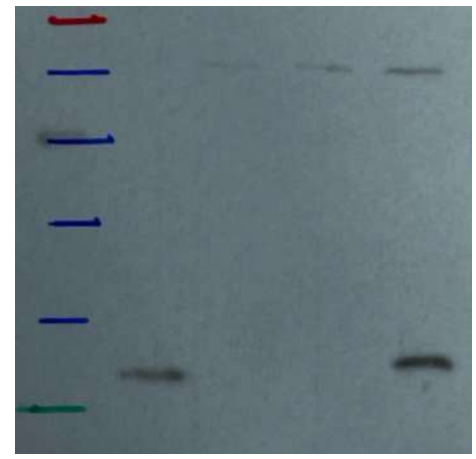

PCM1

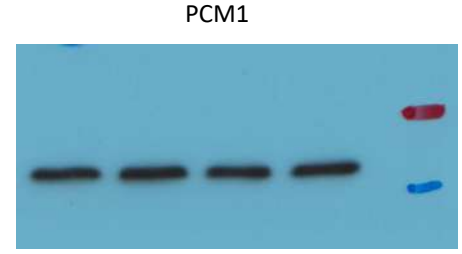

HSC70

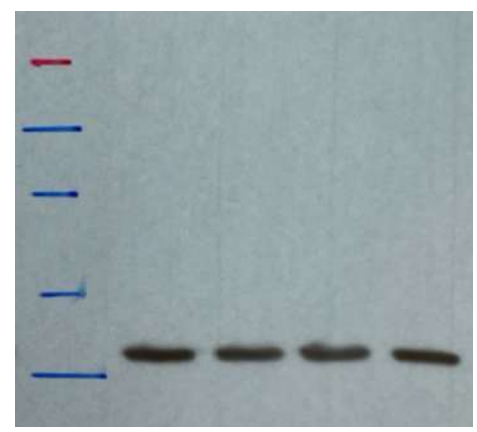

Blots in Fig. S1

C

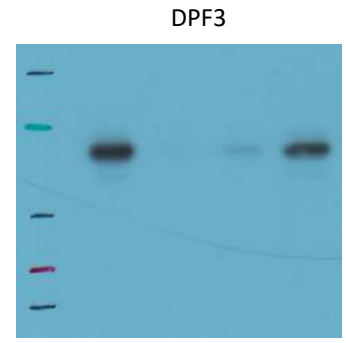

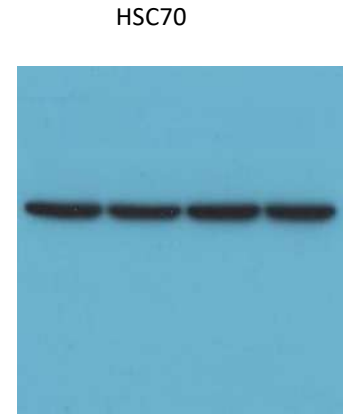

Blots in Fig. S4

B

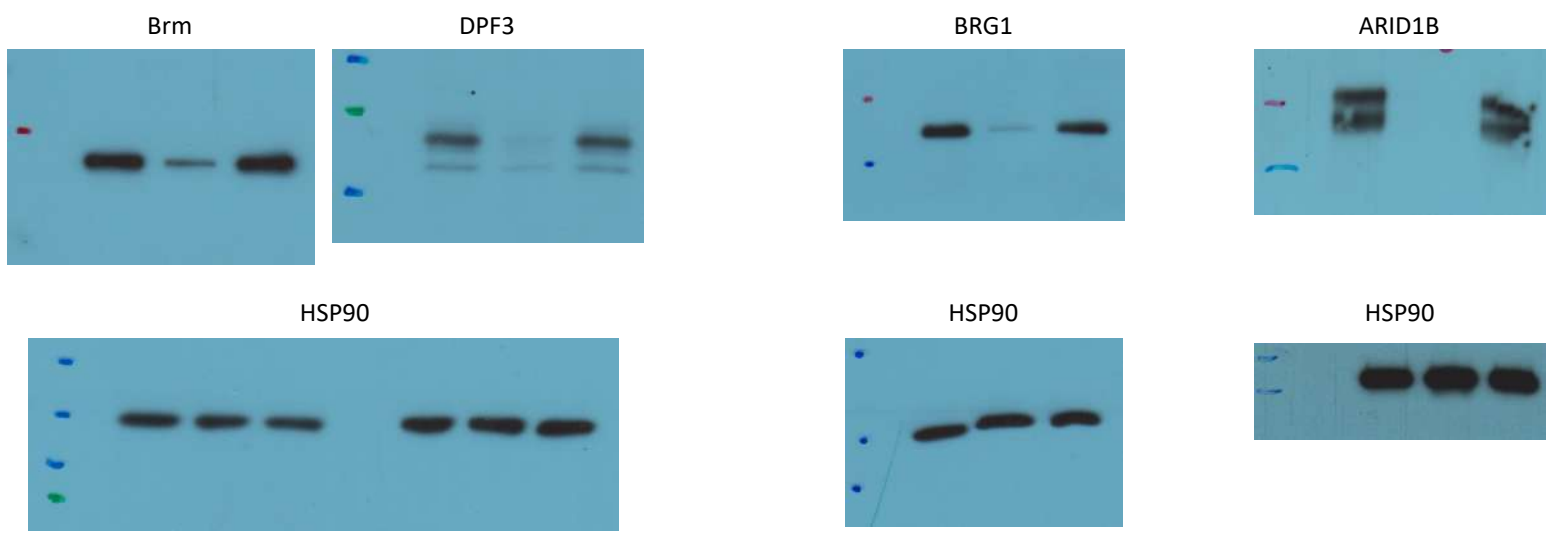

Fig. S6. Blot Transparency

Movie 1. Live-cell imaging of U2OS cells transfected with control siRNA (siCtrl). Cells were transfected for 16 hours using calcium phosphate precipitation method and recovered for 8 hours. Live imaging was then started. Images were acquired every 10 min for a total of 24 hours.

Movie 2. Live-cell imaging of U2OS cells transfected with DPF3 siRNA (si DPF3#1). Cells were transfected for 16 hours using calcium phosphate precipitation method and recovered for 8 hours. Live imaging was then started. Images were acquired every 10 min for a total of 24 hours. DPF3-depleted cells spent an unusually long time in mitosis. They did undergo mitosis and showed induction of post-mitotic apoptotic cell death.

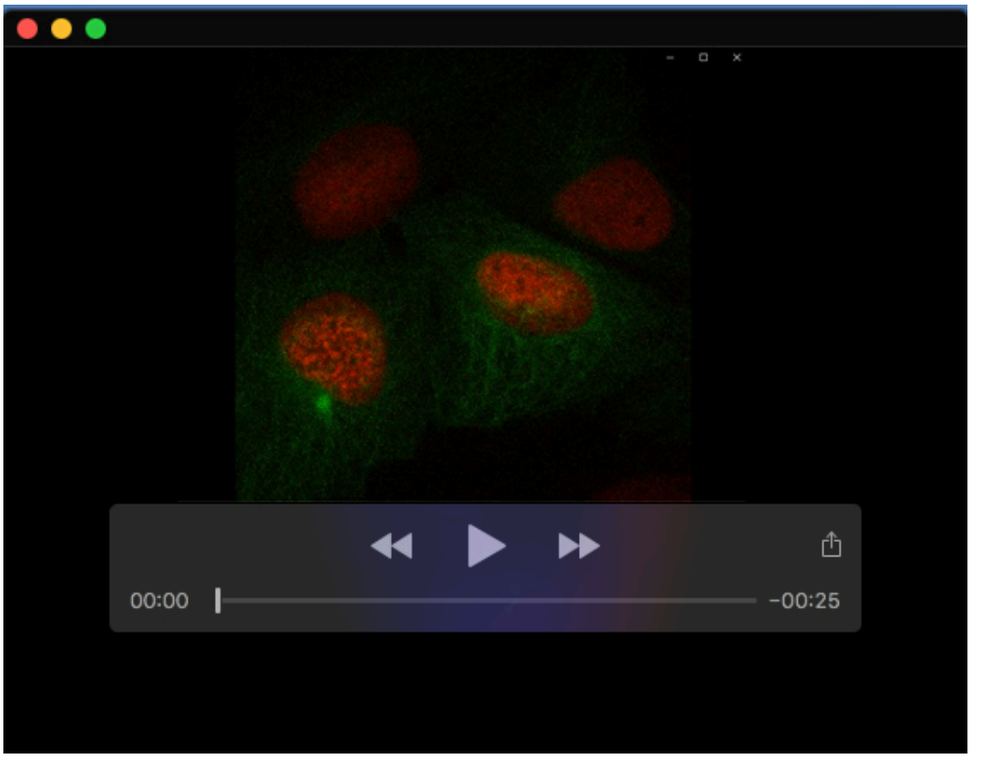

Movie 3. Fluorescent live-cell imaging of H2B-RFP/α-actin-GFP U2OS cells transfected with control siRNA (siCtrl).

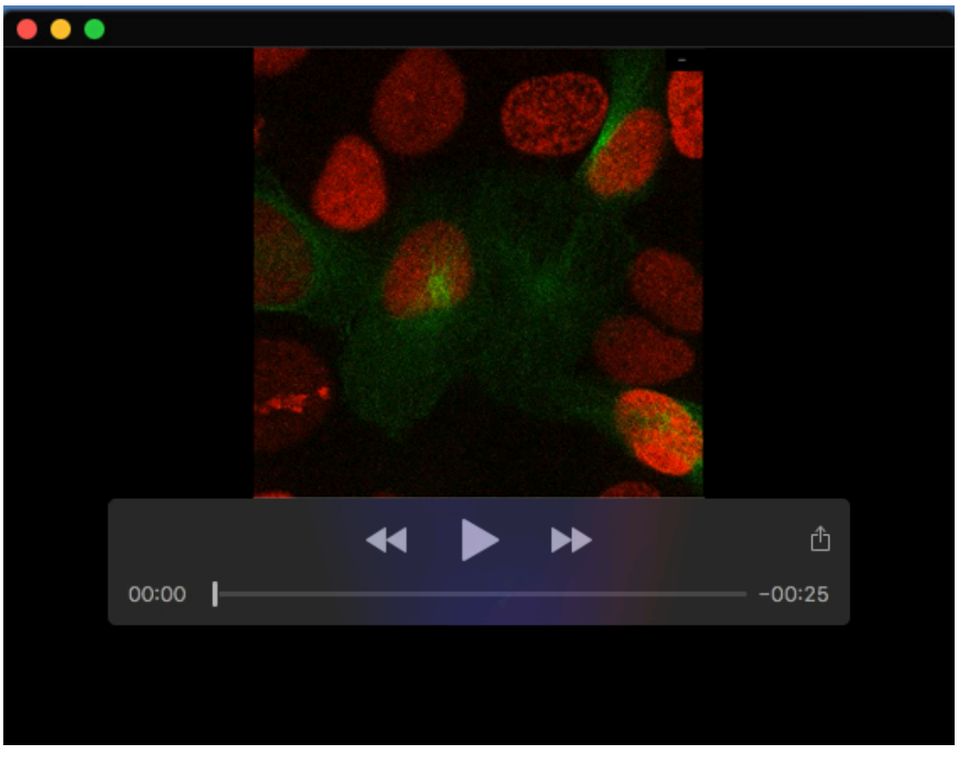

Movie 4. Fluorescent live-cell imaging of H2B-RFP/α-actin-GFP U2OS cells transfected with DPF3 siRNA (si DPF3#1). DPF3-depleted cells exhibited chromosome hyper-oscillations and spent an unusually long time in mitosis.

Journal of Cell Science • Supplementary information

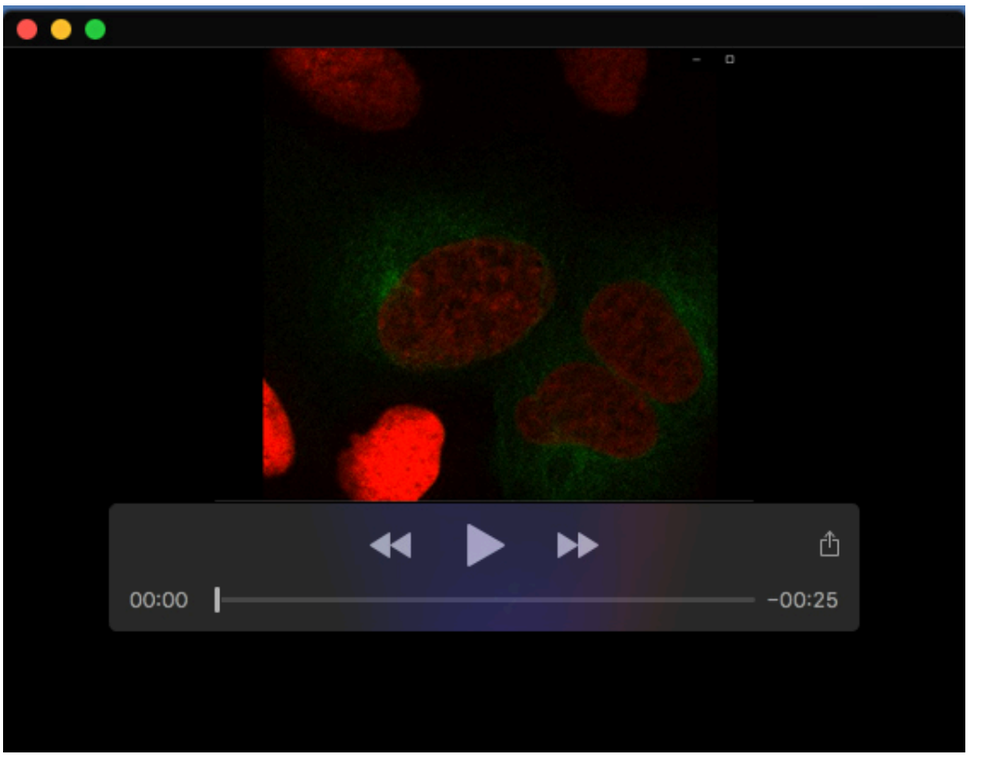

Movie 5. Fluorescent live-cell imaging of H2B-RFP/α-actin-GFP U2OS cells transfected with DPF3 siRNA (si DPF3#1). DPF3-depleted cells exhibited chromosome hyper-oscillations and spent an unusually long time in mitosis.

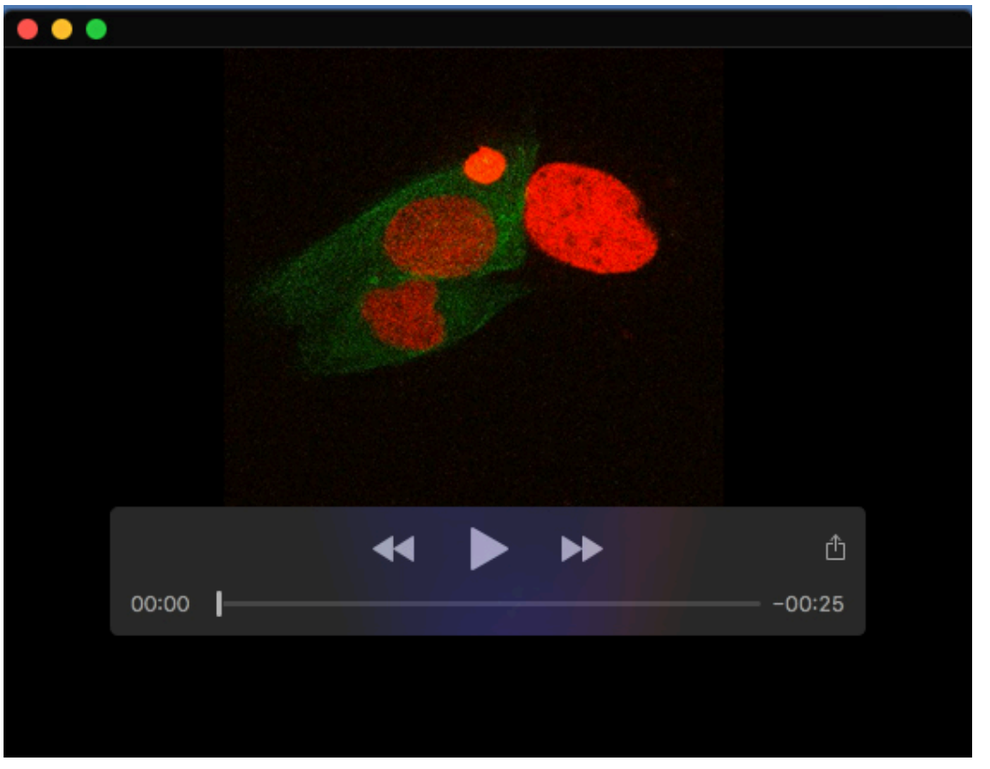

Movie 6. Fluorescent live-cell imaging of H2B-RFP/α-actin-GFP U2OS cells transfected with DPF3 siRNA (si DPF3#1). DPF3-depleted cells did undergo anaphase and subsequent cytokinesis, leading to asynchronous/ unscheduled chromatid separation.

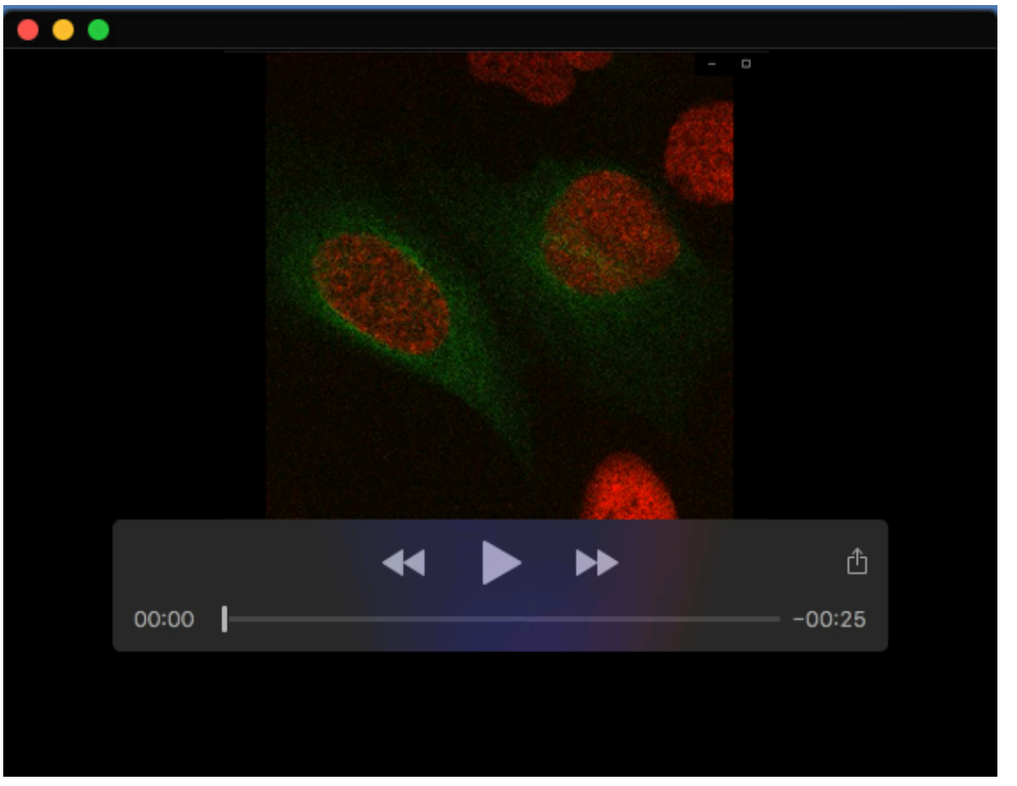

Movie 7. Fluorescent live-cell imaging of H2B-RFP/α-actin-GFP U2OS cells transfected with DPF3 siRNA (si DPF3#1). DPF3-depleted cells did undergo anaphase and subsequent cytokinesis, leading to formation of nuclei with irregular shapes (formation of bi/multi-lobed nuclei).

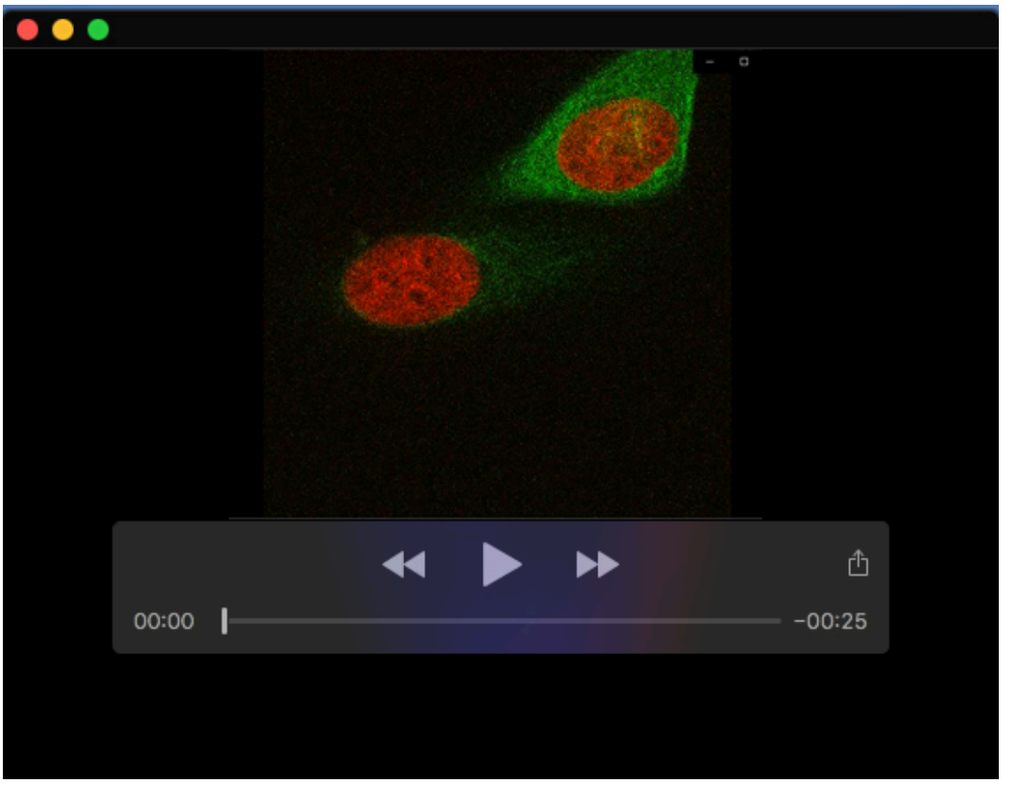

Movie 8. Fluorescent live-cell imaging of H2B-RFP/α-actin-GFP U2OS cells transfected with DPF3 siRNA (si DPF3#1). DPF3-depleted cells showed induction of post-mitotic apoptotic cell death.